ORNL/TM-2021/2273

SCALE Analysis of a Fluoride Salt-Cooled High-Temperature Reactor in Support of Severe Accident Analysis

Friederike Bostelmann
Cihangir Celik
Robert F. Kile
William A. Wieselquist

March 7, 2022

OAK RIDGE National Laboratory

ORNL IS MANAGED BY UT–BATTELLE, LLC, FOR THE U.S. DEPARTMENT OF ENERGY

ORNL/TM-2021/2273

Nuclear Energy and Fuel Cycle Division

SCALE ANALYSIS OF A FLUORIDE SALT-COOLED HIGH-TEMPERATURE REACTOR IN SUPPORT OF SEVERE ACCIDENT ANALYSIS

Friederike Bostelmann
Cihangir Celik
Robert F. Kile
William A. Wieselquist

Date Published: March 7, 2022

Prepared by
OAK RIDGE NATIONAL LABORATORY
Oak Ridge, TN 37831-6283
managed by
UT-Battelle, LLC
for the
US DEPARTMENT OF ENERGY
under contract DE-AC05-00OR22725

CONTENTS

LIST OF FIGURES

LIST OF TABLES

ACRONYMS

2D	two-dimensional
3D	three-dimensional
ARP	Automatic Rapid Processing
BOL	beginning of life
CE	continuous-energy
CPU	central processing unit
EFPD	equivalent full-power day
FHR	fluoride salt-cooled high-temperature reactor
HFP	hot full-power
HTGR	high-temperature gas-cooled reactor
IMSR	Integral Molten Salt Reactor
LWR	light water reactor
MCNP	Monte Carlo N-Particle
MG	multigroup
MSR	molten salt reactor
MSRE	Molten Salt Reactor Experiment
MTIHM	metric ton initial heavy metal
NRC	US Nuclear Regulatory Commission
ORNL	Oak Ridge National Laboratory
PWR	pressurized water reactor
SNL	Sandia National Laboratories
TRISO	tristructural isotropic

ACKNOWLEDGMENTS

Support for this work was provided by the US Nuclear Regulatory Commission (NRC) under Contract IAA 31310019N0012. The authors would especially like to thank program managers Don Algama and Lucas Kyriazidis of the NRC for their support and constructive feedback. Suggestions and comments received from many of our colleagues in ORNL's Nuclear Energy and Fuel Cycle Division and from Nicholas R. Brown (University of Tennessee, Knoxville) are greatly appreciated. The feedback provided by the MELCOR team, in particular from K.C. Wagner (Sandia National Laboratories), David L. Luxat (Sandia National Laboratories), and Jason Schaperow (NRC) was very helpful.

ABSTRACT

As part of a US Nuclear Regulatory Commission–sponsored project to assess the modeling and simulation capabilities for accident progression, source term, and consequence analysis for advanced reactor technologies with SCALE and MELCOR, SCALE was used for the modeling and simulation of a fluoride salt-cooled high-temperature reactor (FHR).

Based on the preconceptual design for a small modular 236 MWth FHR developed by the University of California, Berkeley (PB-FHR-Mk1), a SCALE model of the PB-FHR-Mk1 reactor core was developed. The reactor was modeled at equilibrium state with different fuel compositions in different regions of the reactor. An iterative approach was used to interpolate and mix the burnup-dependent fuel compositions obtained through the depletion calculation of a core slice model. After demonstrating the applicability of SCALE's multigroup (MG) approach for the simulation of the PB-FHR-Mk1, the resulting equilibrium core was studied in terms of the power profile, the flux profile, temperature reactivity coefficients, and the xenon reactivity. Furthermore, the tritium production rate in the salt coolant was determined, and the dependence of the one-group cross sections on the burnup and location in the reactor core was studied.

The results obtained with SCALE were post-processed to provide the MELCOR team with the core inventory and decay heat of the equilibrium core, a zone-wise power profile, temperature feedback coefficients, the tritium production rate, and the xenon worth.

1. INTRODUCTION

The fluoride salt-cooled high-temperature reactor (FHR) is an advanced reactor design currently being developed by the industry; operation of a first demonstration reactor is expected in 2026 [ANS Nuclear Newswire, 2021]. This reactor design combines the tristructural isotropic (TRISO) fuel technology typically used in helium-cooled high-temperature gas-cooled reactor (HTGR) concepts (e.g., HTR-10 [Terry et al., 2007] or PBMR-400 [NEA, 2013]) with liquid salt cooling, which has typically been used in molten salt reactor (MSR) concepts (e.g., the Molten Salt Reactor Experiment (MSRE) [Shen et al., 2019] or the Integral Molten Salt Reactor (IMSR) [Choe et al., 2018]).

Different concepts for FHRs with different fuel component designs have been proposed, including plate fuel [Holcomb et al., 2011], cylindrical fuel compacts [Krishna et al., 2020], and fuel pebbles [Andreades et al., 2016]. The FHR concept studied in this work is the preconceptual design for a small modular 236 MWth *pebble-bed* (PB) FHR reactor developed by the University of California, Berkeley (PB-FHR-Mk1). The PB-FHR-Mk1 is a graphite-moderated pebble-bed reactor cooled by liquid FLiBe (Li_2BeF_4) salt that aims to combine the benefits of continuous refueling with the advantages of liquid salt coolant.

With respect to neutronics modeling, key differences between the PB-FHR under consideration and pebble-bed HTGRs are (1) the liquid salt coolant and (2) the TRISO particle arrangement in the fuel pebble. Liquid salt coolant introduces sources for neutron scattering and absorption into the system. Temperature and density reactivity feedback of the salt coolant must be considered. Because of the salt components lithium and fluorine, the generation of tritium through neutron capture must be modeled; the tritium generation rate is hundreds of times higher than in light water reactors (LWRs). When comparing the energy-dependent neutron flux of an FHR system with the neutron flux of an HTGR and an LWR, the similarity with the HTGR flux in terms of the higher thermal peak is clear (Figure 1). In the fast energy range, the FHR flux shows a smaller peak and additional resonances because of scattering reactions with the salt components (Figure 2).

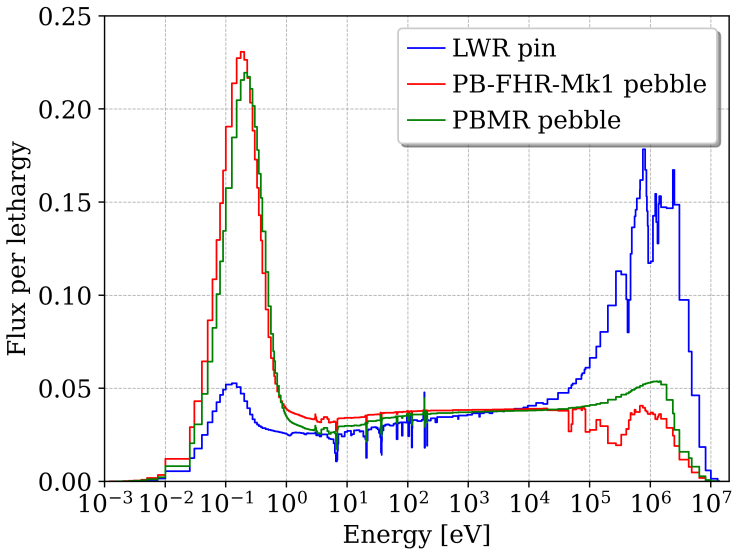

Figure 1. Normalized neutron flux of an LWR fuel pin, a PB-FHR-Mk1 fuel pebble, and a PBMR-400 fuel pebble (all fresh fuel) calculated with SCALE.

The TRISO particle arrangement in the fuel pebble presents another modeling challenge. The FHR fuel pebble diameter is 3 cm, compared to the 6 cm in common HTGR concepts (Figure 3). Furthermore, the

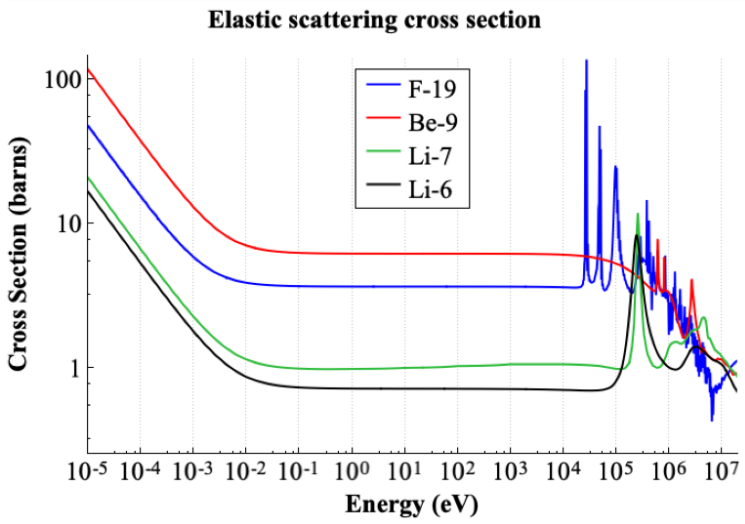

Figure 2. Elastic scattering cross section of FLiBe salt components (ENDF/B-VII.1).

TRISO particles in HTGR pebbles are dispersed throughout the entire sphere and covered by a thin graphite layer. In contrast, the FHR pebbles include an inner graphite sphere which takes up most of the pebble volume. The TRISO particles are located in a 0.2 mm thin layer and are protected by another thin layer of graphite. To achieve the desired high power density, sufficient TRISO particles have to be included per pebble, thus requiring a very high packing fraction of ~40%.

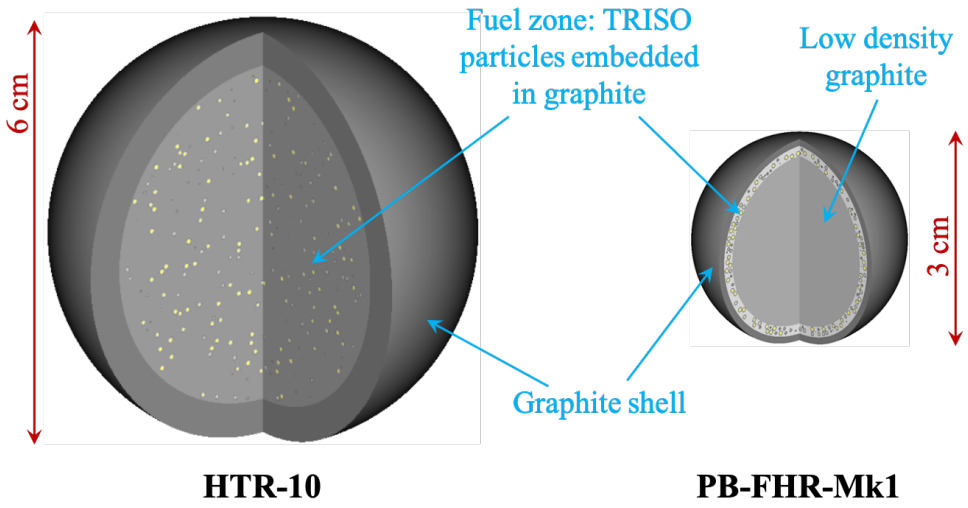

Figure 3. Comparison of HTGR (HTR-10) and FHR (PB-FHR-Mk1) fuel pebbles.

The calculations presented in this report were performed with the SCALE code system [Wieselquist et al., 2020]. For many years, SCALE has been used and continuously improved for the modeling and simulation of double heterogeneous systems in which the fuel component—such as a fuel pebble or cylindrical compact—is comprised of TRISO fuel particles distributed within a graphite matrix [Goluoglu & Williams, 2005, Ilas, 2010, Ilas et al., 2012, Williams et al., 2015, Kim et al., 2021]. Current and emergent SCALE capabilities to address double-heterogeneous systems and the latest verification and validation studies of these methods and data have recently been published [Bostelmann et al., 2020].

To assess the modeling and simulation capabilities for accident progression, source term, and consequence analysis for non-LWR technologies, the US Nuclear Regulatory Commission (NRC) initiated a collaborative project between the NRC, Sandia National Laboratories (SNL), and Oak Ridge National Laboratory (ORNL) [US NRC, 2020]. The SNL team is continuing to develop and use the computer code MELCOR [Humphries et al., 2015] to perform severe accident progression and source term analyses. For these analyses, they rely on the ORNL team to provide fission product and radionuclide inventories, kinetics parameters, power distributions, and decay heat as determined with SCALE.

Following the reports about the SCALE analysis results of the pebble-bed HTGR PBMR-400 [Skutnik & Wieselquist, 2021] and the INL A heat pipe reactor [Walker et al., 2021], this report summarizes the outcome of the SCALE analyses of the PB-FHR-Mk1. A description of the main characteristics relevant for neutronics modeling is followed by a discussion of the applicability of SCALE's multigroup (MG) approach for the simulation of this FHR. This is followed by descriptions of fuel compositions for the different regions in a full FHR reactor core. These fuel compositions are being developed for the state of equilibrium during which fuel pebbles are continuously added and removed from the core such that the average fuel compositions (and consequently the average burnup) in each core region remain approximately the same. This core is then analyzed in terms of the power profile, the flux profile, and temperature reactivity coefficients. The tritium production rate in the salt coolant is presented, and the dependence of the one-group cross sections on the burnup and location in the reactor core is analyzed. All calculations were performed using a development version of SCALE 6.3 in combination with ENDF/B-VII.1 nuclear data libraries. A collection of SCALE input and output files are provided in the public SCALE model repository associated with this project: `https://code.ornl.gov/scale/analysis/non-lwr-models-vol3`.

The results obtained with SCALE were post-processed to provide the MELCOR team with the core inventory and decay heat of the equilibrium core, a zone-wise power profile, temperature feedback coefficients, the tritium production rate, and the xenon worth. While most data was provided in simple text files or spreadsheets, the core inventory and decay heat was provided directly in MELCOR's DCH-file (decay heat file). Based on a recent enhancement, SCALE can provide inventory data through an inventory interface ("ii") file which is emitted in standard JSON format. The obtained inventory interface file was easily converted into the DCH-file so that no further post-processing was needed on the MELCOR side for this data. Based on data provided from SCALE, the MELCOR teams simulated an anticipated transient without SCRAM, a station blackout, and a loss-of-coolant accident as reported in [Wagner et al., 2021a, Wagner et al., 2021b].

2. FHR DESCRIPTION

The FHR system studied in this work is the preconceptual design for a small modular 236 MWth reactor developed by the University of California, Berkeley. The Mark-1 (Mk1) PB-FHR design was developed within the scope of a US Department of Energy project to establish the technical basis to design, license, and commercially deploy FHRs [Andreades et al., 2014]. The key characteristics as provided in [Andreades et al., 2014] are presented in Table 1.

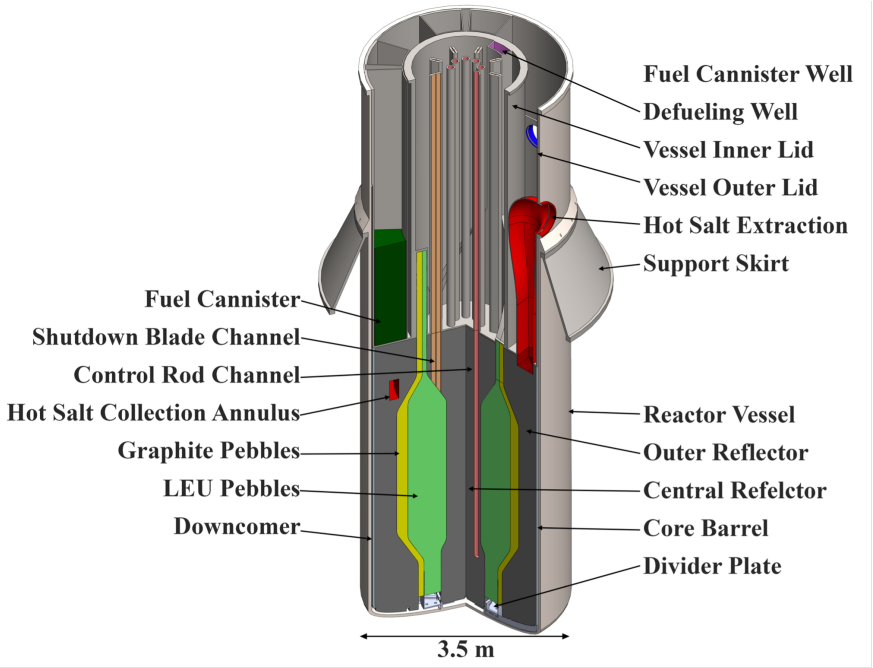

Figure 4. PB-FHR-Mk1 full core model [Andreades et al., 2014].

The PB-FHR-Mk1 design combines the HTGR fuel form with liquid fluoride salt coolant in a graphite-moderated environment. The annular core is filled with 470,000 fuel pebbles surrounded by 218,000 graphite moderator pebbles, and the core is contained in graphite reflector structures (Figure 4). The pebbles travel from the bottom of the core to the top. On average, a fuel pebble completes 8 passes through the core before reaching its final discharge burnup of 180 GWd/metric ton initial heavy metal (MTIHM). As in an HTGR, the fuel pebbles contain TRISO particles distributed in a graphite matrix. The FHR pebbles contains an average of 4,730 TRISO particles, which corresponds to ~1.5 gU per pebble. However, the fuel pebbles in the FHR are significantly smaller (3 cm diameter compared with 6 cm the HTR-10, for example). The fuel particles within the FHR pebble are distributed in a shell-like fuel region compared with a spherical fuel region in HTR-10. The fuel region in the FHR pebble is 1.5 mm thick, and the packing fraction of the TRISO particle in this shell is 40% (Figure 5).

The fuel material is UCO, with an enrichment of 19.9 wt% ^{235}U. The coolant salt is FLiBe, which is a mixture of LiF and BeF_2. Core inlet and outlet temperatures are approximately 600 and 700°C, respectively, and the fuel temperature ranges between 700 and 800°C. The average thermal power per fuel pebble is 500 W. Burnups reaching up to 180 GWd/MTIHM are intended. Reactivity control is achieved using control rods and blades containing boron carbide [Andreades et al., 2014].

A SCALE model of this reactor has been developed using a Monte Carlo N-Particle (MCNP) model published by Cisneros [Cisneros, 2013] as a starting point.

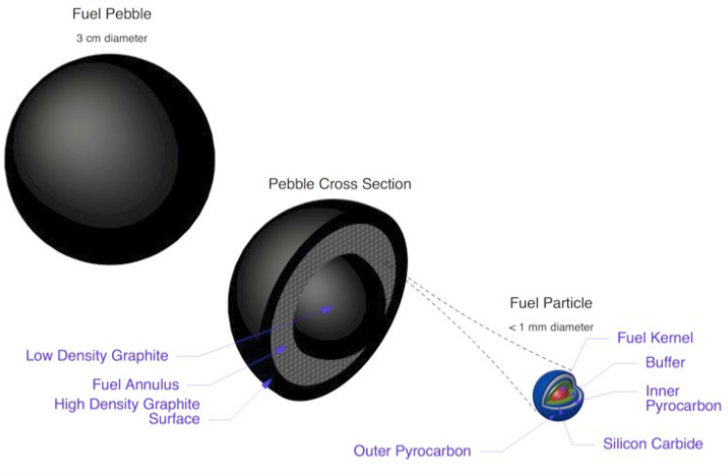

Figure 5. PB-FHR-Mk1 fuel pebble model [Andreades et al., 2014].

Table 1. Key characteristics of the PB-FHR-Mk1 [Andreades et al., 2014]

Description	Value
Reactor power (MWth)	236
Coolant	FLiBe salt
UCO fuel kernel density (g/cm^3)	10.5
Uranium enrichment (wt% ^{235}U)	19.9
Fuel kernel radius (mm)	0.20
Fuel particle coating layer materials (starting from kernel)	Buffer/PyC/SiC/PyC
Fuel particle coating layer thickness (mm)	0.100/0.035/0.035/0.035
Number of particles in pebble	4,730
Particle packing fraction in fuel pebble	40%
Radius of fuel pebble (cm)	1.5
Radius of fuel zone in pebble (cm)	
Inner	1.25
Outer	1.40
Graphite matrix and fuel pebble outer shell density (g/cm^3)	1.73
Graphite density of reflector structures (g/cm^3)	~1.76
Graphite density of boronated carbon bricks (g/cm^3)	~1.53
Number of pebbles in the core	
Fuel pebbles	470,000
Dummy pebbles	218,000
Pebble packing fraction	60%
Core dimensions (cm)	
Inner reflector radius	35
Outer fuel pebble region	105
Outer graphite pebble region	125
Volume of active fuel region (m^3)	10.4
Average pebble thermal power (W)	500
Average pebble discharge burnup (GWd/MTHM)	180
Average pebble full-power lifetime (years)	1.40

3. VERIFICATION OF SCALE'S MG APPROACH FOR AN FHR FUEL PEBBLE

SCALE has a unique capability for the modeling and simulation of double-heterogeneous systems—systems with TRISO particles distributed in a fuel component which is itself part of a lattice—based on a simple user input and using MG cross sections. This approach enables the rapid generation of input files describing the system of interest, and it also facilitates calculations with a much reduced computation time compared to models which include explicitly modeled TRISO particle and models which use continuous-energy (CE) cross sections.

Many studies have been performed to verify SCALE's MG approach for double-heterogeneous systems. These studies address code-to-code comparisons, as well as calculation of benchmark experiments [Sunny & Ilas, 2010, Ilas et al., 2012, Bostelmann et al., 2020, Kim et al., 2021]. Since the fuel pebble of the FHR has a different geometry than that of previous pebble concepts (as described in the Introduction)—in particular, an annular shell of TRISO particles instead of a smaller sphere filled with particles—it was decided to perform additional verification analyses by comparing MG to CE reference calculations for a single fuel pebble. Additionally, this analysis explored multiple methods to realize modeling of the particles in the fuel pebble for CE calculations to demonstrate the challenges and the approximations required for various modeling approaches, even for CE analysis.

3.1 SCALE FUEL PEBBLE MODEL DEVELOPMENT

A single FHR-PB-Mk1 pebble model was used to investigate the impact of the TRISO particle modeling in a fuel pebble on the infinite multiplication factor k_∞ in eigenvalue calculations, and on k_∞ and the fuel composition in depletion calculations. Although the fuel pebbles are randomly distributed in the FHR core for a given packing fraction, a square lattice model representing the simple cubic lattice structure with a single pebble surrounded by FLiBe salt coolant and reflecting boundary conditions was assumed to create a simple model and to focus on TRISO particle distributions inside the pebble. Various models for CE and MG calculations were studied to investigate the accuracy and performance of the simulations.

The developed pebble models were mainly categorized based on used nuclear cross section formats such as MG and CE. Models using the CE cross section libraries were further categorized based on the arrangement of TRISO particles in the fuel zone in either a regular lattice or through a random distribution. A similar study was performed by Bostelmann et al. [Bostelmann et al., 2020] using an HTR-10 pebble to observe the impacts of the TRISO particle modeling on the infinite multiplication factor.

The FHR-PB-Mk1 pebble was modeled following the description in Chapter 2. The TRISO particle model as used in the CE models is presented in Figure 6. The different pebble modeling approaches are presented in the following.

The four FHR fuel pebble models in a cubic lattice geometry that were developed for this study are as follows:

1. CE model using a square lattice, allowing particle clipping
2. CE model using a square lattice without particle clipping
3. CE model using using a random particle distribution
4. MG model using SCALE's double-het treatment

Material temperatures in the pebble models are divided into three categories to represent transitions in operating conditions:

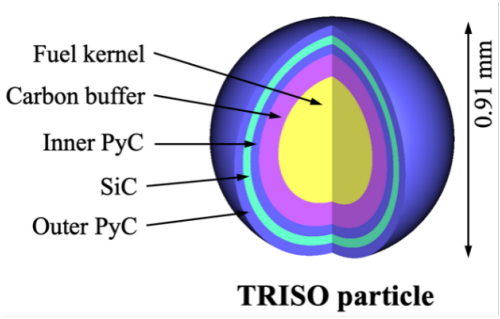

Figure 6. SCALE TRISO particle model.

- ***cold***: all materials are at 300 K
- ***warm***: all pebble materials are at 900 K while the coolant is at 600 K
- ***hot***: fuel kernel is at 1,003.15 K, coatings are at 973.15 K, graphite at the pebble center is at 983.15 K, outer shell graphite is at 957.15 K, and coolant is at 923.15 K

All models developed for this analysis have the same amount of fuel in the pebble. Some geometry and density adjustments were applied as described in detail below to effectively construct models within a given set of constraints. While the calculations reported here were only performed with ENDF/B-VII.1 nuclear data libraries, comparisons of calculations using ENDF/B-VII.0, ENDF/B-VII.1, and ENDF/B-VIII.0 data, and analyses concerning the impact of thermal moderator scattering data on HTGR systems were previously reported [Bostelmann et al., 2020].

3.1.1 CE MODEL: SQUARE PARTICLE LATTICE WITH CLIPPING

The simplest approach for developing a CE model is to use an infinite lattice of TRISO particles and to place this lattice into the fuel region, thus permitting the clipping of particles by the surfaces defining the fuel region. In the present study, a square lattice model was employed. The lattice pitch was adjusted to keep the total fuel mass and volume consistent with the specifications. A segmented view of the square lattice model with clipped TRISO particles is shown in Figure 7.

An algorithm was developed to adjust the particle lattice pitch of this model as follows:

- Requirements:
  - Include the target fuel mass in the pebble
  - Include a fuel volume equal to the sum of 4,730 fuel kernel volumes
  - Do not alter the fuel and coating layer densities or thicknesses
- Implementation:
  - Initialize the particle lattice pitch from the number of particles
  - Obtain volumes via KENO-VI volume calculation
  - Compare the calculated fuel volume with the target fuel volume
  - Calculate a new particle lattice pitch based on the volume comparisons of the previous iterations
  - Repeat the iterations until converged
- Iteration conditions, convergence criteria, and results:

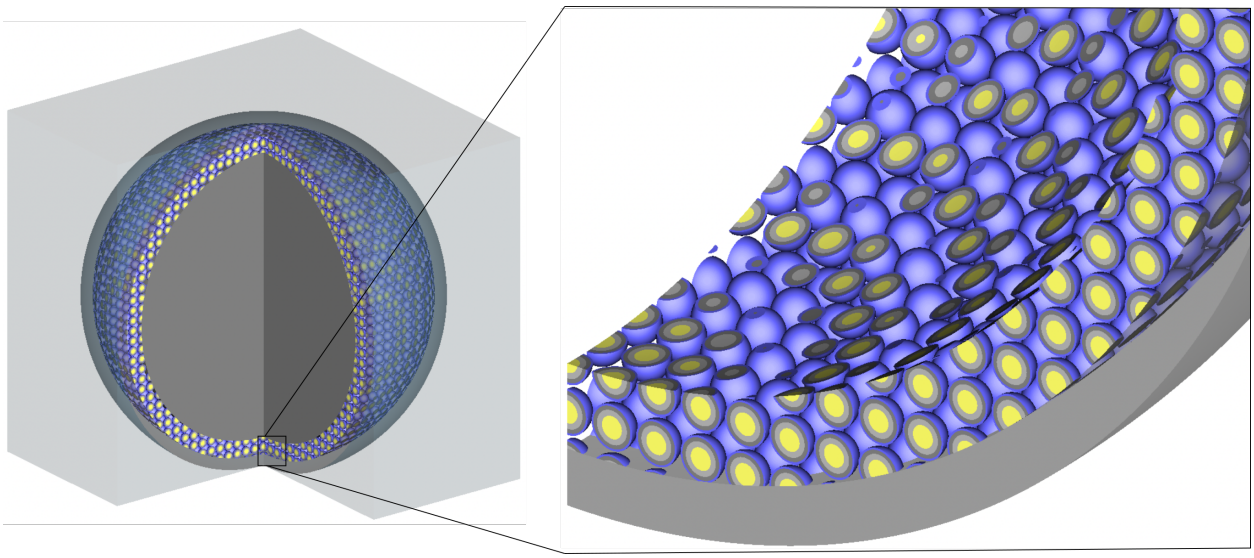

Figure 7. SCALE CE pebble model: TRISO particles arranged in a square lattice, clipped by the surrounding surfaces.

  - Statistical error in volume calculation <= 0.01%
  - Pitch range increments of 10−6 cm
  - Target difference to reference fuel volume <= 0.0002%
  - Local particle packing fraction determined from the lattice pitch is 39.45%

3.1.2 CE MODEL: SQUARE PARTICLE LATTICE WITHOUT CLIPPING

The square particle lattice model without clipping is similar to the clipped model described above, but it avoids particle clipping by explicitly placing particles at lattice positions that allow the entire particle to be contained in the fuel zone. To be able to pack the correct number of particles into the fuel region, densities and thicknesses of the TRISO particle coating layers had to be adjusted and a small lattice pitch had to be used. All TRISO particle coating layer thicknesses are compressed by 22% to be able to fit the correct number of fuel particles into the pebble. Due to the small lattice pitch, the local particle packing fraction was reduced to 74% which is much larger than the local packing fraction of 39.45% in the clipped model. A segmented view of the square lattice model without clipped TRISO particles is shown in Figure 8.

For this model, an algorithm was developed to adjust the particle lattice pitch and particle coating densities:

- Requirements:
  - Include the target fuel mass in the pebble
  - Do not permit TRISO particles to be clipped by surrounding surfaces
- Implementation:
  - Initialize the particle lattice pitch from the number of particles
  - Adjust all coating layer densities by increasing or decreasing the layer thicknesses by the same ratio
  - Adjust the pitch range by increasing or decreasing the lattice pitch

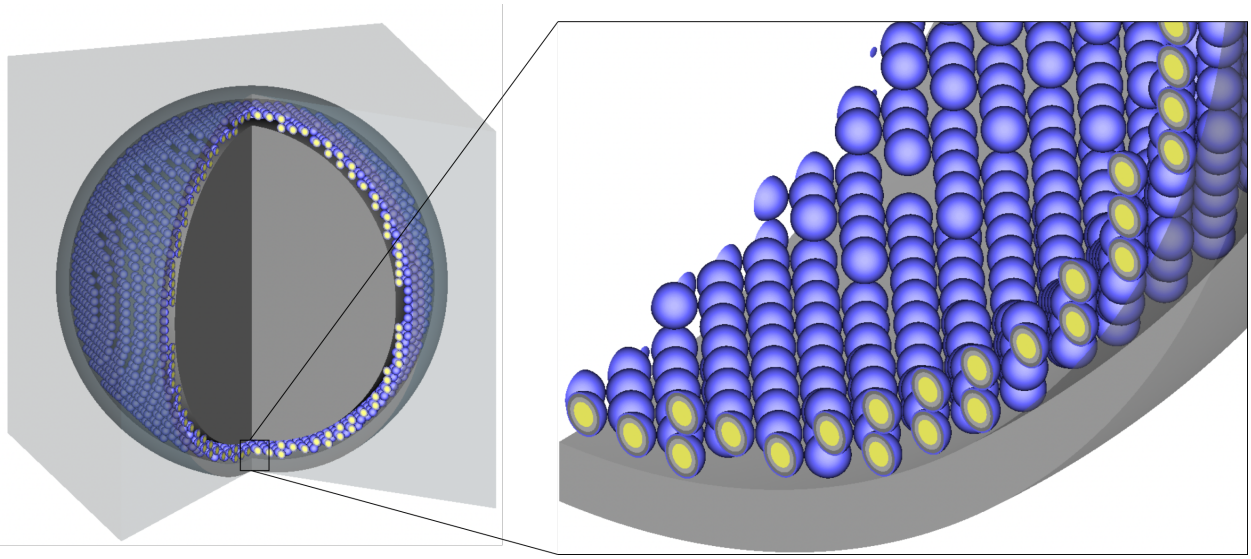

Figure 8. SCALE CE pebble model: TRISO particles arranged in a square lattice without clipping.

  - Check that explicitly placed particles in the lattice avoid particle clipping
  - Repeat the process until a viable configuration is achieved
- Results:
  - Coating layers' thicknesses (buffer/IPyC/SiC/OPyC) are decreased by 22%
  - The density of each layer is increased to preserve the mass
  - The density of the graphite matrix is decreased to preserve the mass
  - The local packing fraction is ~74% based on the original outer TRISO radius (~52% based on 22% decreased outer TRISO radius)

3.1.3 CE MODEL: RANDOM PARTICLE DISTRIBUTION

This model represents the most realistic modeling of a fuel pebble, but it presents the biggest modeling challenges of all the developed CE pebble models in this study, and it requires the most computational resources. The coordinates of all TRISO particles were randomly sampled and accepted (1) if the outermost surface of the TRISO particle did not intercept with any other TRISO particle, and (2) if the outermost surface of the TRISO particle did not intercept with the inner or outer spheres defining the fuel region. These requirements guaranteed that particles would not be clipped. Each TRISO particle coating layer had to be compressed by 15% to allow placement of the target number of TRISO particles in the pebble's fuel region. If random sampling did not yield an acceptable configuration after a predefined number of trials, then a compactor algorithm was used to randomly pull each placed particle toward the center of the pebble. Furthermore, a coarse cuboidal lattice laid over the fuel region to contain a subset of TRISO particles in each lattice element. This addition of an overlaid coarse lattice has previously been demonstrated to accelerate the Monte Carlo particle transport calculations [Bostelmann et al., 2020]. A segmented view of the random TRISO particles model is shown in Figure 9.

An algorithm was developed to adjust the particle lattice pitch and particle material densities to develop this model:

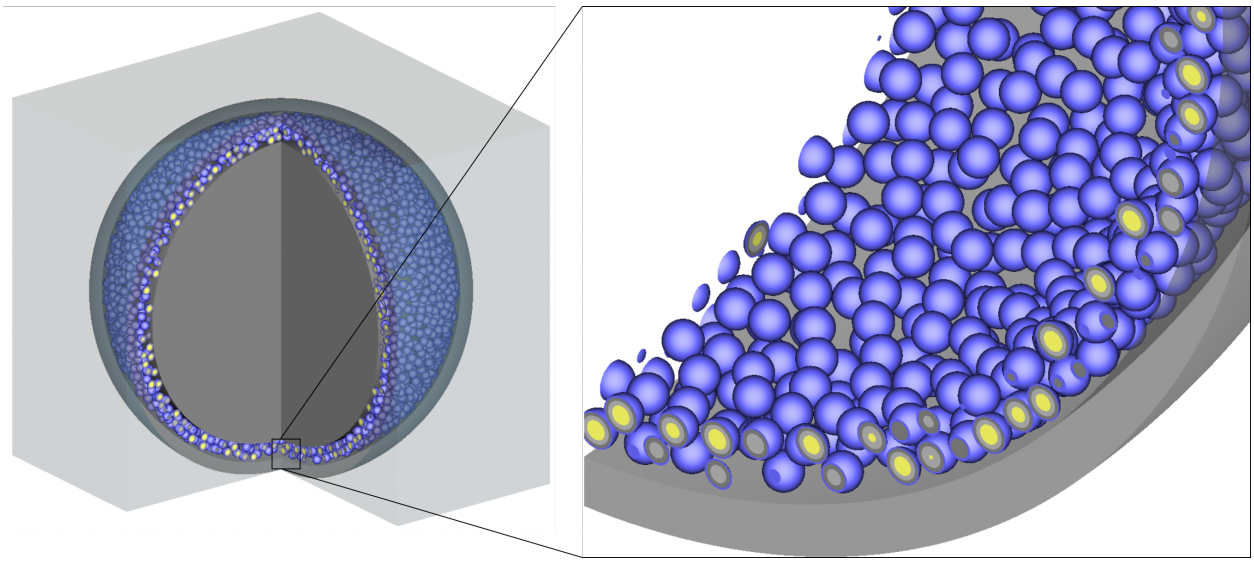

Figure 9. SCALE CE pebble model: TRISO particles randomly distributed.

- Requirements:
  - Include the target fuel mass in the pebble
  - Do not permit TRISO particles to be clipped by surrounding surfaces
- Implementation:
  - Sample the centers of particles and accept locations if no clipping occurs
  - If no variable configuration is found, then pack all particles by pulling them towards the center of the pebble
  - If no viable configuration is found after compacting, then reduce all layer thicknesses by the same ratio and adjust their densities
  - After the required number of particles is successfully placed, place particles in corresponding lattice elements
- Results:
  - Coating layers' thicknesses (buffer/IPyC/SiC/OPyC) are reduced by 15%
  - The densities of all layers are increased to preserve the mass
  - The density of the graphite matrix is decreased to preserve the mass
  - Average fuel packing fraction of ~40%
  - 10 SCALE models with different random TRISO particle distributions

It is noted that SCALE 6.3 will include a new feature for modeling stochastic geometries that is enabled via a new geometry block *randomgeom* when using the Monte Carlo code Shift. This block enables compact descriptions of double-heterogeneous CE models by users. Like the *double-het* feature for MG calculations, this new feature only requires a few parameters. With the *randomgeom* block, TRISO particles are automatically randomly placed inside a specified fuel region during code execution or model visualization. Although this feature is available in development versions of SCALE 6.3 and was used for the HTR-10 pebble study [Bostelmann et al., 2020], it was intentionally not used in this study because of its limitation on the packing fraction and because the geometry of the spherical shell as a region definition vector for the fuel region is not yet supported.

3.1.4 MG MODEL

SCALE has a unique approach for MG calculations of double-heterogeneous systems, often abbreviated with *double-het* approach. The cross section self-shielding treatment for the fuel region is automatically performed based on a simple user input describing the details for the TRISO particles and the pebble [Williams, 2011]. The result are problem-dependent cross sections for the fuel region which the user can place with a simple identifier into the respective fuel region. A segmented view of the MG model is shown in Figure 10.

MG calculations are desired especially for double-heterogeneous systems because of the simple geometry definitions and the neutron transport calculation with group-wise (MG) neutron cross sections instead of continuous point-wise (CE) cross sections, which require a much longer computation time. However, MG approximations can result in small biases. For example, in terms of the multiplication factor, a MG bias of less than 300 pcm was previously shown for a HTGR fuel pebble, and an even smaller MG bias was shown for two HTGR full-core systems [Bostelmann et al., 2020].

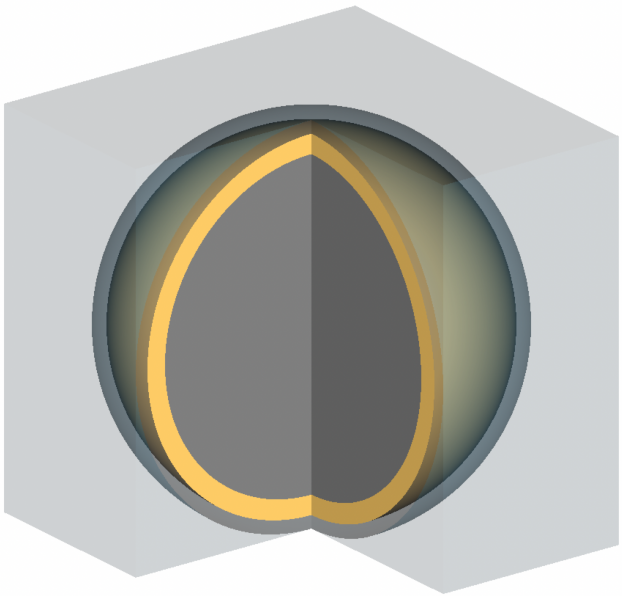

Figure 10. SCALE pebble model: MG model with the double-heterogeneous mixture (i.e., problem-dependent cross sections) placed in the fuel region (orange).

3.2 EIGENVALUE CALCULATIONS

All developed single pebble models with reflecting boundary conditions and with the aforementioned temperature profiles were simulated using SCALE's Monte Carlo code KENO-VI. The CE random distribution model was chosen as the reference model because it represents the most realistic model of an actual FHR pebble. The random distribution model was duplicated with 10 different TRISO particle distributions in the fuel zone of the pebble, and an average multiplication factor and performance metrics are reported in this study. Remaining models have been simulated with 10 different random number seeds for the Monte Carlo particle transport calculations, and the averaged metrics and reactivity difference from the reference model were reported to assess the models' accuracy and performance. A Linux Beowolf cluster with the Red Hat Enterprise Linux 7 operating system and a central processing unit (CPU) of Intel® Xeon® Gold 6226R processors was used to run all simulations. Models were run on dedicated computing nodes, with 32 processors allocated for each individual job, that is for every combination of temperature and random seed or particle distribution. Computed infinite multiplication factors, k_∞, for all pebble models, are given in Table 2.

The unclipped lattice model is the closest approximation to the random distribution model, and the computed multiplication factors also reflect this similarity, independent of the temperature profile used in the model, with a maximum reactivity difference of -30 pcm for the warm condition. Although the same CE libraries were used, the reactivity difference is much larger for the clipped model, with a lower bias of -255 pcm for the cold case, with an underestimation ranging up to -309 pcm for the hot case. This bias can be explained by the clipped TRISO particles in the pebble's narrow fuel zone, as seen in Figure 7. Only three rows of TRISO particles can fit into the spherical shell fuel zone, with the first and the last rows being clipped. In addition, increased resonance escape probability as a result of cross section Doppler broadening also adversely impacts the bias from clipping, yielding even higher biases for higher temperatures. The observed bias from TRISO clipping is smaller here compared to a HTGR pebble with a spherical fuel region reported by Ilas et al. [Ilas et al., 2012]. In case of the HTGR pebble, a smaller fraction of clipped TRISO particles is close to the edge of the contiguous fuel zone, whereas the TRISO particles in the FHR pebble are included in a narrow region in which kernels are clipped at both the inner and outer bounding surfaces of the fuel zone.

The MG model yielded better multiplication factor results than the clipped model, with a maximum reactivity difference of -229 pcm for the cold condition and -164 pcm for the hot condition. Regardless of how they were treated, all CE lattice models and the MG model underestimated the multiplication factor with various levels of biases. The impact of higher temperatures resulted in opposite trends in the reactivity biases between the CE and MG models. CE models showed higher biases at higher temperatures, whereas the MG double-het treatment yielded lower biases.

The performance of the reference model with random TRISO distribution was deprived because of the explicit modeling of each TRISO particle in the pebble, which caused excessive floating point operations during geometry tracking of neutrons. Memory utilization of all models was dominated by the nuclear data and required around 600 MB of physical memory per simulation. CE pebble models using lattices, with or without the TRISO clipping, achieved speedups of approximately 5 times that of the CE random particle model. This is mostly caused by fast geometry tracking in the repeated structures in SCALE algorithms. The MG model was the fastest running model, achieving speedups ranging from 20 to 25 times faster. The main reason for the superior performance of the MG calculation is that the pebble model was simplified to a homogenized fuel region represented by a single set of MG cross sections instead of containing explicit TRISO particle definitions, thus yielding high-speed geometry tracking.

Table 2. FHR pebble model multiplication factor k_∞ results using ENDF/B-VII.1 data

Model	Random distribution	Unclipped array		Clipped array		Double heterogeneous	
	k_∞ [a,b]	k_∞ [a,c]	$\Delta\rho$ [pcm] [a,c,d]	k_∞ [a,c]	$\Delta\rho$ [pcm] [a,c,d]	k_∞ [a,c]	$\Delta\rho$ [pcm] [a,c,d]
Cold	1.52539(6)	1.52470(7)	-30(4)	1.51948(6)	-255(4)	1.52007(6)	-229(4)
Warm	1.45775(7)	1.45715(7)	-28(4)	1.45122(7)	-309(5)	1.45378(6)	-187(4)
Hot	1.44765(7)	1.44722(7)	-21(5)	1.44120(7)	-309(5)	1.44422(7)	-164(5)

[a] Values in parentheses are 1σ statistical uncertainties in pcm, 1 pcm = 0.00001, for Monte Carlo simulations. For example 1.23456(7) is 1.23456±0.00007

[b] Average value of 10 individual realizations with separate random particle distribution

[c] Average value of 10 individual realizations with separate random number seeds for the Monte Carlo simulations

[d] Reactivity difference with respect to the random distribution model in pcm

Table 3. Performance metrics for the FHR pebble model

Model	Random distribution		Unclipped array		Clipped array		Double heterogeneous	
	CPU Time (min) [a,b]	Peak Memory (MB) [a,b]	CPU time (min) [a,c]	Peak memory (MB) [a,c]	CPU time (min) [a,c]	Peak memory (MB) [a,c]	CPU time (min) [a,c]	Peak memory (MB) [a,c]
Cold	74 (2)	456 (40)	15 (1)	530 (18)	15 (1)	533 (9)	3 (0.2)	668 (74)
Warm	80 (2)	600 (8)	17 (1)	560 (13)	17 (1)	558 (10)	4 (0.2)	689 (6)
Hot	81 (2)	694 (23)	17 (1)	653 (16)	17 (1)	668 (29)	4 (0.3)	745 (21)

[a] Values in parentheses are 1σ statistical uncertainties in performance metrics. For example 123(4) is 123±4

[b] Average value of 10 individual realizations with separate random particle distribution

[c] Average value of 10 individual realizations with separate random number seeds for the Monte Carlo simulations

3.3 DEPLETION CALCULATIONS

A depletion calculation was performed to investigate the reactivity and fuel inventory by using the single pebble models described above. The temperature distribution corresponding to the *hot-condition* model was applied. Based on the a average pebble power of 500 W, and by considering an average mass of 1.5 g heavy metal, a specific power of 333 MW/MTIHM was applied [Andreades et al., 2014]. To reach the average pebble discharge burnup of 180 GWd/MTIHM, six depletion steps (15, 45, 75, 105, 135, and 180 GWd/MTIHM) were requested. While smaller depletion steps at the beginning of life are usually chosen to capture the xenon buildup at beginning of life, only few depletion steps were considered in this analysis. This simplification is justified since the present study focused on the performance comparison between the various FHR fuel pebble models, but not on the analysis of the actual results of the depletion calculation. The depletion calculations were performed with the TRITON sequence of a SCALE 6.3 development version using ENDF/B-VII.1 cross section libraries.

Figure 11 shows the burnup-dependent infinite multiplication factors k_∞ obtained as the average of 10 realizations of the random TRISO distribution model. This model is considered as the reference for comparisons. As in the eigenvalue calculations with fresh fuel, the CE unclipped lattice model shows good agreement with the CE reference model. A maximum reactivity difference of -62 pcm was observed for the unclipped model at 75 GWd/MTIHM. Of all the models, the CE clipped pebble model showed the highest discrepancy in the multiplication factor results, ranging up to -492 pcm reactivity bias at 105 GWd/MTIHM. The MG calculations resulted in consistent behavior as for the eigenvalue calculations, with a maximum reactivity bias of -259 pcm at 45 GWd/MTIHM. Although the maximum reactivity biases were observed at different burnup levels, the CE lattice and MG models showed consistent behavior, increasing to more negative biases around the mid-discharge burnup level, and decreasing biases toward the end-of-life discharge burnup levels.

The development of the fuel inventory for selected nuclides throughout the depletion is shown in Figure 13 for the reference model. Comparisons of the CE lattice nuclide densities and MG models to the CE reference model are shown in Figure 13 through Figure 15. Excellent agreement with a difference of less than 1% was observed between the reference and the CE unclipped lattice model throughout the depletion cycle; the maximum error occurred at around 135 GWd/MTIHM. The CE clipped lattice model had a maximum nuclide density difference of 2% for ^{235}U and 5% for ^{241}Am at the end of the burnup cycle. Similar trends for ^{239}Pu and ^{241}Pu, with differences of around 4%, were observed. The remaining isotopes had less than 2% differences at the discharge burnup level. The MG model yielded less than 3% differences in the nuclide densities throughout the depletion cycle. However, unlike the CE lattice models, which typically underestimated the nuclide inventory, the MG model produced a wide spread from underestimating to overestimating some of the fission products and actinides such as ^{134}Pu, ^{153,154,155}Eu, ^{154,155}Gd, and ^{245}Cm. This behavior is most likely caused by the 252-group representation of the cross sections in the MG library, which was optimized for the analysis of LWR systems with lower discharge burnup values. The maximum differences in the discharge inventory were observed in the CE clipped lattice model. But all models agreed within 5% for the discharge actinide inventory, with ^{235}U having a difference of less than 2%.

The computation times for running the depletion model are 45 times faster than the times for the CE lattice models and 60 times faster than the CE random distribution model computation times.

3.4 CONCLUSIONS

Pebble models have been developed and analyzed to investigate the impact of TRISO particle modeling for the PB-FHR-Mk1 fuel pebble. Eigenvalue and depletion calculations were performed to assess the accuracy and performance of the models using SCALE methods and data. The random TRISO distribution model with CE libraries was chosen as the reference model because it represents the actual model more accurately than the others. All other results from different models were compared to the results of this reference model.

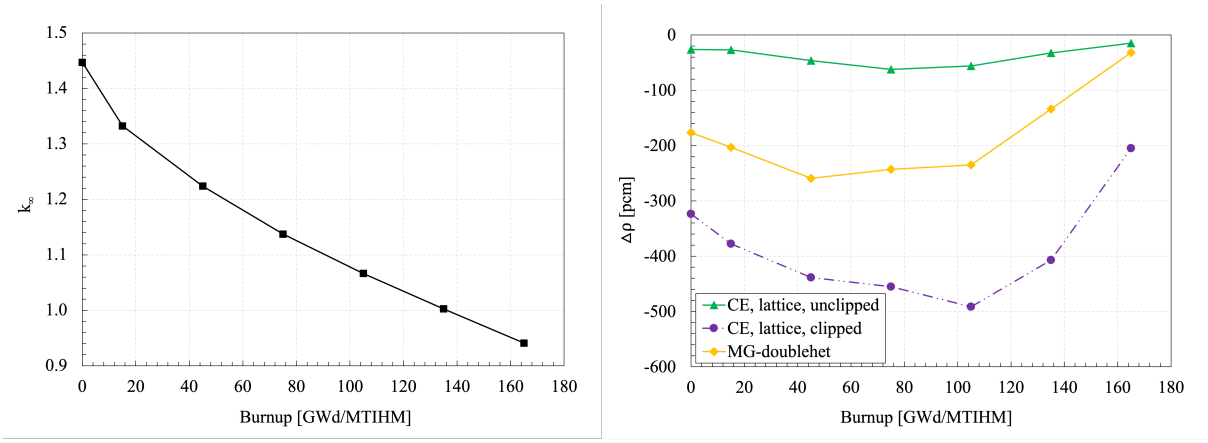

Figure 11. Burnup-dependent k_∞ of random particle model and reactivity differences of other models.

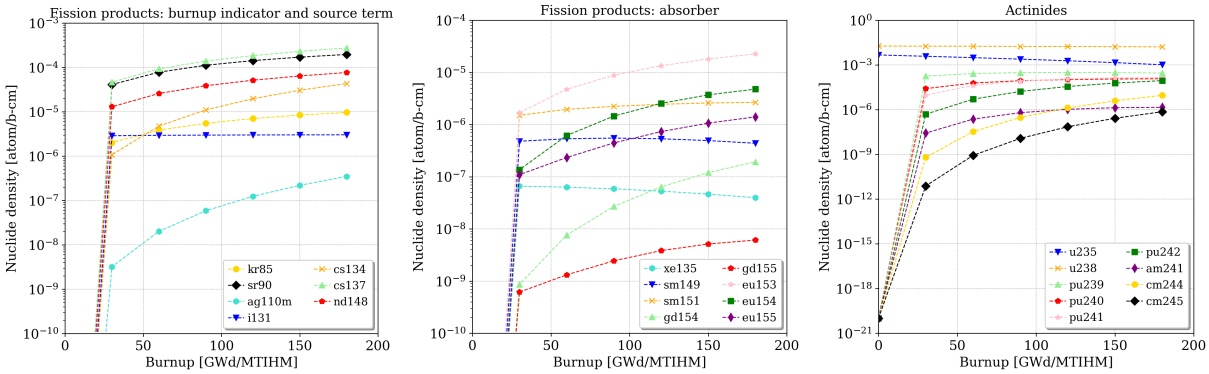

Figure 12. Nuclide densities determined with the CE random particle model.

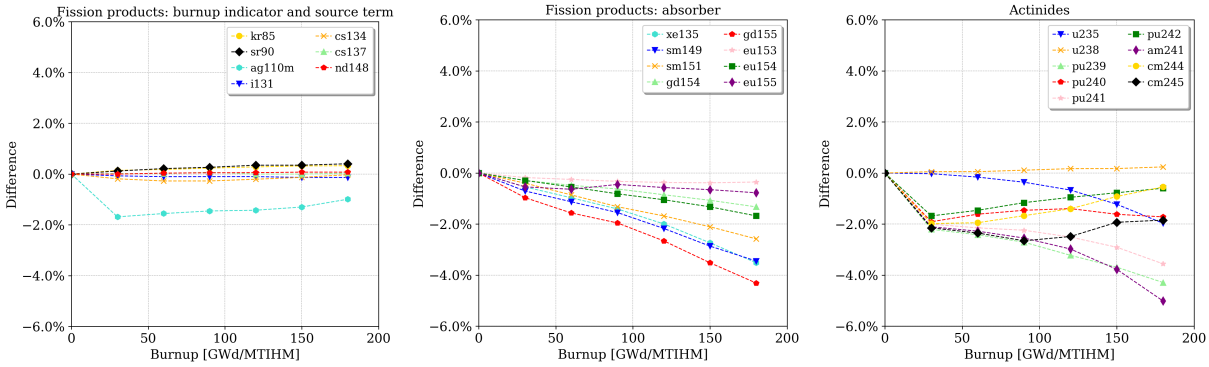

Figure 13. Difference between nuclide densities: CE lattice clipped vs. CE random.

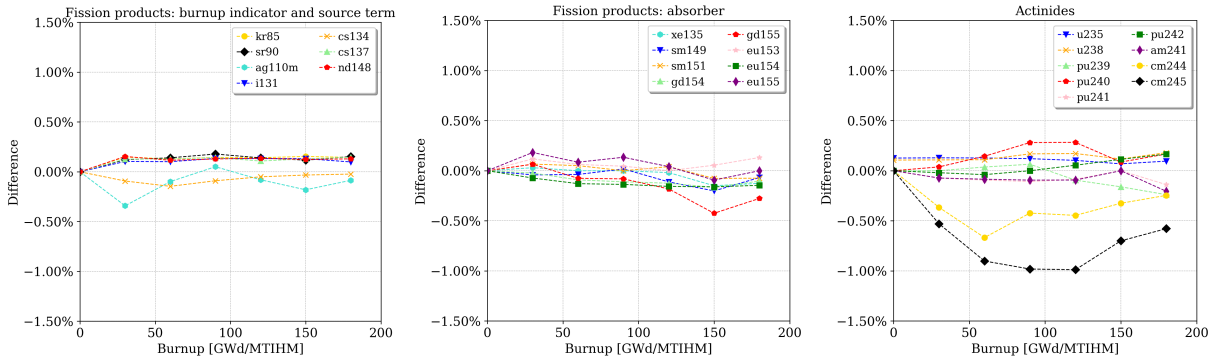

Figure 14. Difference between nuclide densities: CE lattice non-clipped vs. CE random.

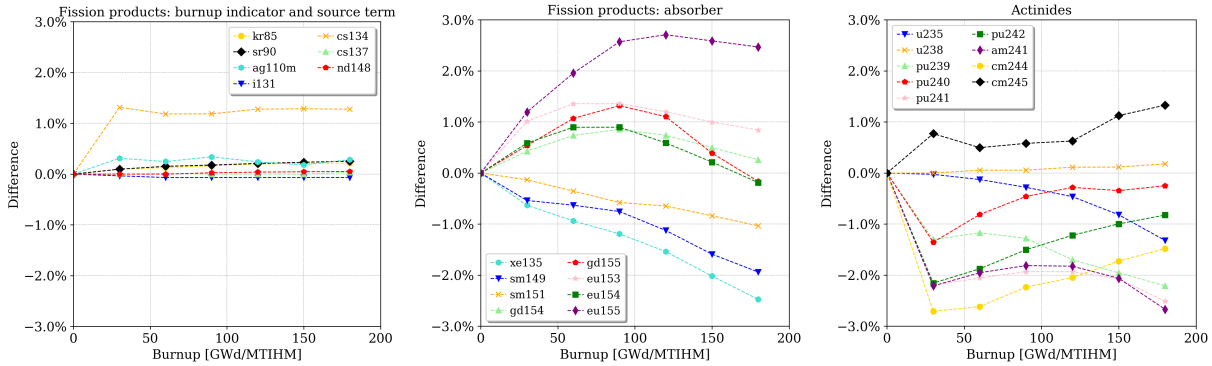

Figure 15. Difference between nuclide densities: MG vs. CE random.

The CE unclipped lattice model yielded the closest results in all analyses, followed by the MG model. Although the CE clipped lattice model offers user-friendly modeling and quick simulation times, it has relatively higher reactivity biases of up to -309 pcm in eigenvalue calculations, and it underestimated the discharge fuel inventory by as much as 5%. Despite an increased modeling effort, it is recommended that CE models are developed by avoiding TRISO particle clipping at the boundaries of the spherical-shell fuel region. While a model with random particle locations is the model closest to reality, lattice models offer faster computation times with a factor of 5 in eigenvalue calculations and a factor of 2 in depletion calculations.

The MG model provided the best performance regarding flexibility of modeling and computation time, achieving reasonable reactivity biases with a maximum of -229 pcm in eigenvalue calculations and below 3% differences in discharge fuel inventory while yielding calculation speedup factors on the order of 20 for eigenvalue and 60 for depletion calculations.

Based on the excellent performances obtained for these fuel pebble analyses with SCALE's MG approach, all further analyses presented in the following sections were conducted based on models using this MG approach. Although the models generated for the studies presented in the following sections were larger than a fuel pebble, the excellent performance of the pebble depletion calculations indicates that SCALE's MG approach can be used for this type of geometry under different neutron spectra. The cumulative effects of the MG bias during depletion were minor, despite the (unrealistic) spectrum hardening during depletion in the small reflected pebble cell.

4. GENERATION AND ANALYSIS OF AN EQUILIBRIUM FHR CORE

After several years of operation, an FHR operates in an equilibrium state in which fuel pebbles that have reached the final discharge burnup after approximately eight passes through the core are constantly replaced by fresh fuel pebbles. At this stage, the FHR core contains a mixture of pebbles at different stages of burnup. The average pebble burnup is increasing with increasing core height because the pebble flow path goes from the bottom to the top of the reactor. But the average burnup and fuel composition in each zone of the reactor remain approximately the same.

For severe accident analyses—in which the decay heat plays a particularly important role—the equilibrium state is more limiting than the state of a start-up core or any configuration approaching an equilibrium state. The average burnup at equilibrium is greater than the burnup of any core having more fresh fuel pebbles, and the decay heat tends to increase with increasing burnup. To provide MELCOR with realistic data for an FHR reactor during operation, a SCALE model of the full PB-FHR-Mk1 reactor core at the state of equilibrium was developed. Based on this model, further analyses of power distribution, decay heat, temperature coefficients, tritium production, and xenon worth were conducted.

It is noted here that the presented approach to determine equilibrium core fuel compositions is one of many possible approaches (see [Skutnik & Wieselquist, 2021] for an overview of the most common tools and approaches). It should be emphasized that if one can predict the neutron flux spectrum and magnitude a pebble will experience as a function of time (properly accounting for standard thermal neutron self-shielding effects), then the inventory (and decay heat) simulations will be of high quality. A more detailed approach could consider all pebbles individually and simulate their individual travel paths with the correct spectral conditions and power level calculated at a large number of snapshots in time as the pebbles traverse the core. This would be prohibitively expensive for equilibrium core calculations. Even if one initiated the calculations with an approximation for inventory of recirculated pebbles (in contrast to simulating the entire core lifetime and multi-year approach to equilibrium), one would need multiple realizations of equilibrium accounting for uncertainty in where pebbles land when entering the core, and how they flow through the core and change directions as they drag and shear against other pebbles. So one would likely need many realizations of this type of simulation to understand an average or most likely equilibrium configuration. Pebbles will most likely not have individual serial numbers and thus tracking individual pebbles in reality will be impossible. Pebble burnup monitoring systems will assess whether a pebble may be recirculated or should be discharged. Therefore it makes more sense to pursue pebble inventory methods which focus on average behavior and provide straightforward ways to assess sensitivity and uncertainty. In this way we can develop insights on the likely distributions within a batch of pebbles.

4.1 DEVELOPMENT OF AN EQUILIBRIUM CORE

As described in Section 2, the annular core of the PB-FHR-Mk1 reactor is filled with 470,000 fuel pebbles which travel from the bottom of the core to the top. On average, a fuel pebble completes eight passes through the core before reaching its final discharge burnup of 180 GWd/MTIHM. This means that at any time during the reactor's operation, a mixture of pebbles at different burnups is included in each axial zone.

To create a representative model of the PB-FHR-Mk1 for the generation of core inventory and decay heat for use in further analysis with MELCOR, a model with an approximate fuel inventory corresponding to a core's equilibrium-state was developed. A flowchart of the iterative approach followed here is shown in Figure 20. Changes in the power profile due to control rod movements are not considered in this approach. The control rods are fully withdrawn for all presented full core simulations. Figure 16 presents a three-dimensional (3D) visualization of the full PB-FHR-Mk1 core model, and Figure 17 shows a two-dimensional vertical cut

through the core model to indicate the axial and radial zones that are referenced in the following description of the approaches.

This approach is based on burnup-dependent fuel compositions which were obtained through depletion of surrogate fuel pebbles in a two-dimensional (2D) slice model of the reactor (Figures 18 and 19). The goal was to deplete a number of pebbles at different radial locations in the slice model under spectral conditions similar to the conditions that the pebbles would experience while traveling through a reactor core. Instead of depleting all fuel pebbles in the slice, only a set of surrogate fuel pebbles at different radial locations was depleted (fuel pebbles highlighted in red in Figure 18). The composition of all other fuel pebbles (lilac) was assumed not to change during depletion. These "non-depletable" fuel pebbles contain a core-average fuel composition which is updated after every iteration as part of the convergence of the representative conditions. While the non-depletable fuel pebbles provide representative spectral conditions as the fuel pebbles would experience in the reactor from the other fuel pebbles in the equilibrium core at various stages of burnup, the different radial locations of the surrogate fuel pebbles account for the different travel paths through the reactor core: close to the inner reflector, next to the graphite pebbles/outer reflector, or in the middle of the fuel pebble region.

The axial height of the slice model was chosen to ensure retention of the correct packing fraction of the pebbles in the annular core. Reflective axial boundary conditions and vacuum radial boundary conditions were applied. Based on the analyses of different pebble lattices and the impact of pebble clipping on the PBMR-400 reactor in [Skutnik & Wieselquist, 2021], the pebbles in the PB-FHR-Mk1 were modeled in a dodecahedral lattice and pebble clipping was permitted. The depletion calculations were performed using SCALE's TRITON sequence with the Monte Carlo code KENO-VI for the neutron transport calculation. The fuel pebbles were depleted with a specific power of 333 MW/MTIHM.

4.1.1 OUTER ITERATION 1: CONSTANT POWER

In the first approach (*outer iteration 1*) to obtain representative fuel compositions of an equilibrium core, the fuel region was divided into 10 axial zones of equal volume, and the following conditions were applied:

- The pebbles are exposed to the same neutron flux in each axial zone.
- Each zone is composed of equal fractions of pebbles at different passes.
- The burnup increases by 22.5 GWd/MTIHM each time a pebble travels through the reactor.

Inner iterations

In the first inner iteration, fresh fuel was applied in both the depletable and non-depletable fuel pebbles. Based on the given specific power of 333 MW/MTIHM and the given discharge burnup of 180 GWd/MTIHM, the first depletion calculation was performed for 540.54 days. A core-average fuel composition was then determined by averaging the compositions of the depleted fuel pebble at different burnups, as described below. For the second inner iteration, this core-average fuel composition was applied in all non-depletable fuel pebbles. Because power in the slice model is generated from all fuel pebbles (i.e., both the depletable and non-depletable fuel pebbles), as well as through capture reactions in non-fuel regions, the final discharge burnup of the surrogate fuel pebbles was close to the given discharge burnup of 180 GWd/MTIHM, but not equal. The discharge burnup and depletion time from the first inner iteration were used to calculate a new depletion time for the second iteration.

The depletion calculation was then repeated, starting with fresh fuel in the surrogate fuel pebbles, but with new spectral conditions based on the changed composition in the non-depletable pebbles for a new total depletion time. Using this depletion calculation, a new core-average fuel composition and a new depletion

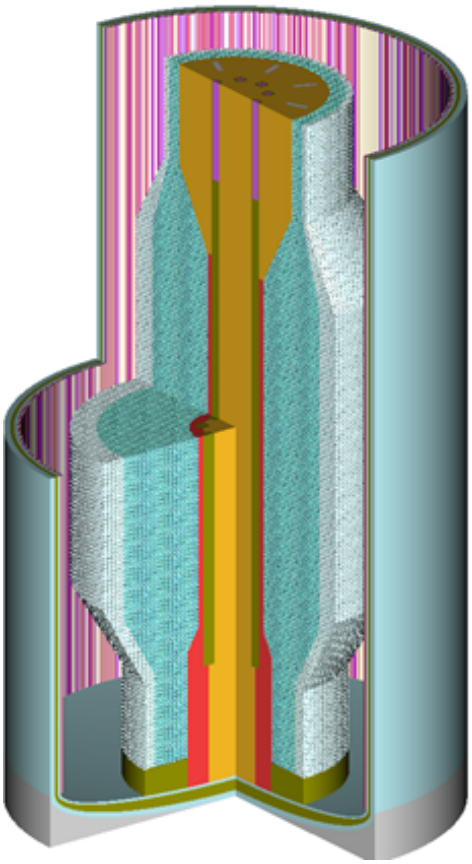

Figure 16. 3D visualization of the SCALE PB-FHR-Mk1 model.

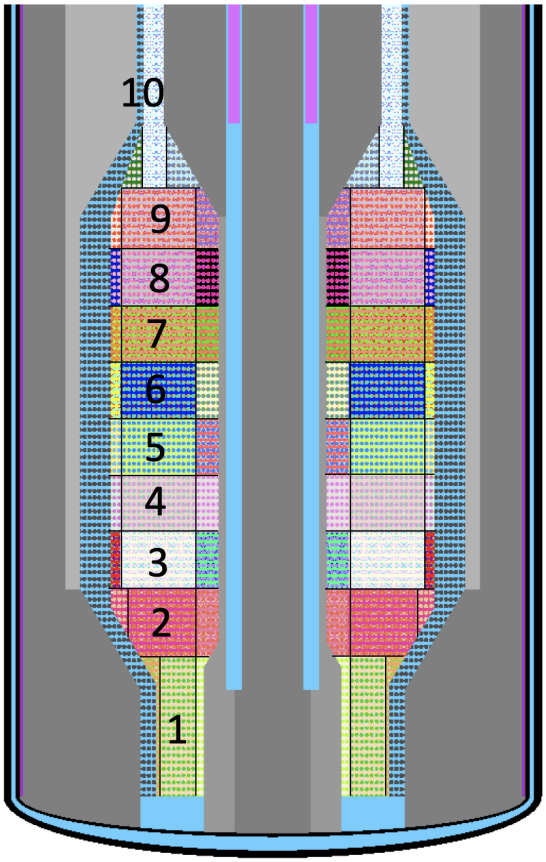

Figure 17. SCALE PB-FHR-Mk1 model highlighting the axial and radial fuel zones.

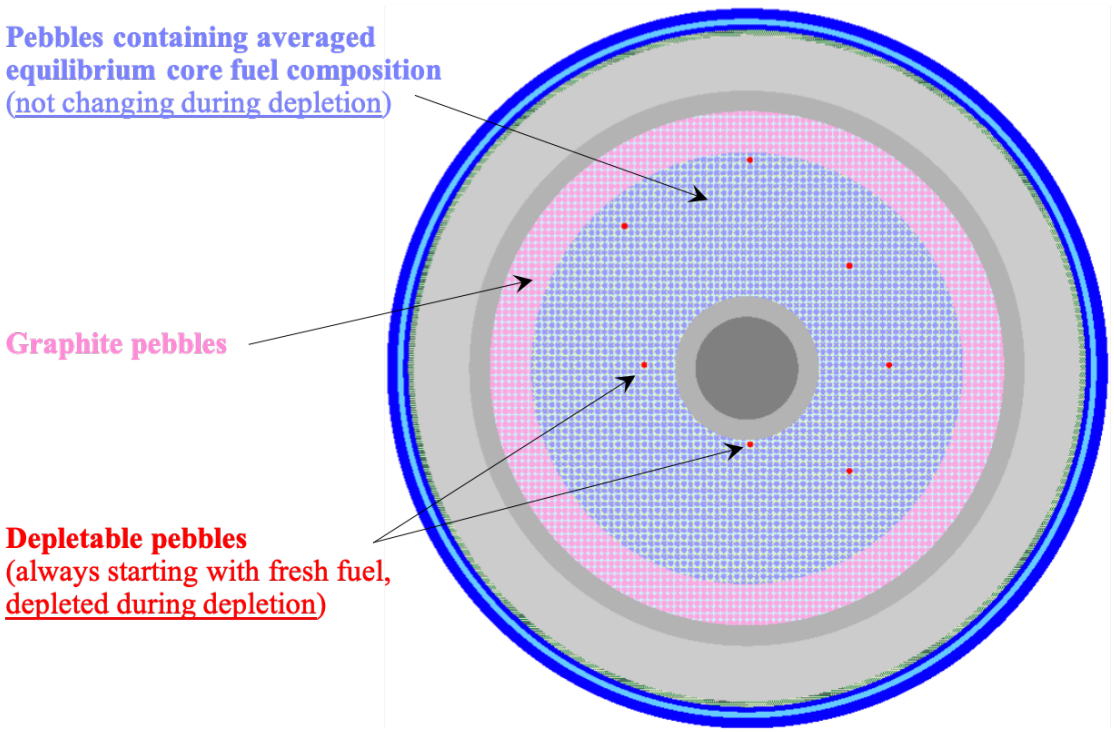

Figure 18. PB-FHR-Mk1: horizontal view of the slice model used for the depletion calculations. The non-depletable fuel pebbles are displayed in lilac, the depletable fuel pebbles in red, the dummy graphite pebbles in pink, the graphite structure in gray, the absorber pins in green, and the outer structure in blue.

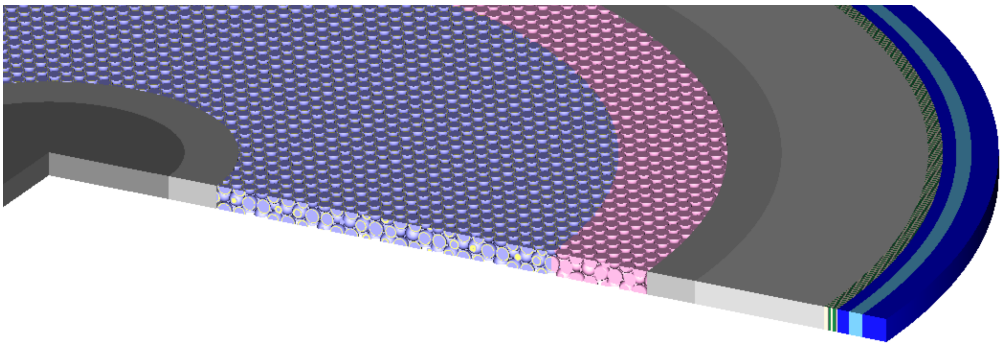

Figure 19. PB-FHR-Mk1: 3D view of the slice model used for the depletion calculations.

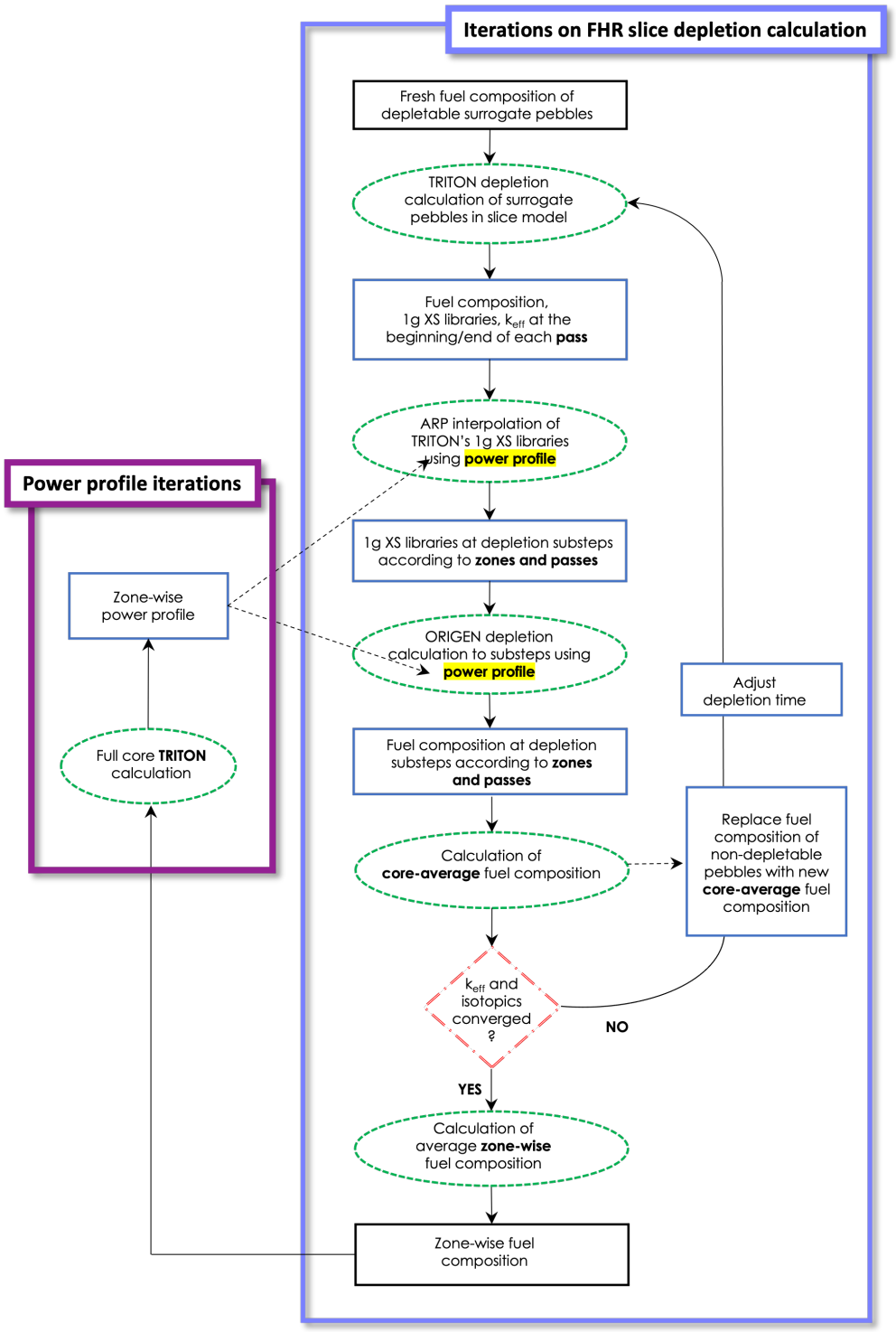

Figure 20. Flowchart showing the process to determine fuel compositions in the individual fuel zones.

time were determined for use in the following iteration. This process was repeated until k_{eff} and the core-average densities of important nuclides reached convergence, meaning that these values were no longer changing significantly between one iteration and the next iteration. At the same time, the final discharge burnup converged to a value close to the desired discharge burnup. After convergence was reached, the fuel compositions at different burnups from the last iteration were used to calculate average fuel compositions for each zone in the core.

Calculation of zone-wise fuel compositions

The average fuel composition in each of the individual fuel pebble regions was calculated by averaging the fuel compositions at different burnups. Each fuel pebble travels eight times through 10 axial zones of the reactor until it reaches the final burnup. Based on the above listed assumptions, a burnup map for the individual axial zones considering the eight passes was created (as displayed in Table 4). Since TRITON provided the ORIGEN binary concentration file (f71-file containing material compositions) and the ORIGEN binary library file (f33-file containing the transition matrix of the material) at a limited number of burnup steps from the slice depletion calculation, at first the Automatic Rapid Processing (ARP) module was used to interpolate the f33-files to the middle of the desired burnup steps, and ORIGEN was then used calculate the fuel compositions at the desired burnup steps. The fuel composition of a pebble in a zone during a particular pass was assumed to correspond to the fuel composition at a burnup in the middle of the zone.

The average fuel composition of an axial zone was calculated by averaging the zone's fuel compositions during the different passes. For example, Table 4 shows that axial zone 3 contains fuel pebbles at burnups of 5.6, 28.1, 50.6, 73.1, 95.6, 118.1, 140.6, and 163.1 GWd/MTIHM. Averaging the fuel compositions at these burnups yields the average fuel composition in zone 3. Core-average compositions were determined through averaging the fuel compositions of all axial zones.

Table 4. Fuel pebble burnup (GWd/MTIHM) in the middle of each axial zone depending on the pass through the core for outer iteration 1 with constant power. See Figure 17 for the location of the axial zones in the core.

	Pass through the core							
Axial zone	1	2	3	4	5	6	7	8
10	21.4	43.9	66.4	88.9	111.4	133.9	156.4	178.9
9	19.1	41.6	64.1	86.6	109.1	131.6	154.1	176.6
8	16.9	39.4	61.9	84.4	106.9	129.4	151.9	174.4
7	14.6	37.1	59.6	82.1	104.6	127.1	149.6	172.1
6	12.4	34.9	57.4	79.9	102.4	124.9	147.4	169.9
5	10.1	32.6	55.1	77.6	100.1	122.6	145.1	167.6
4	7.9	30.4	52.9	75.4	97.9	120.4	142.9	165.4
3	5.6	28.1	50.6	73.1	95.6	118.1	140.6	163.1
2	3.4	25.9	48.4	70.9	93.4	115.9	138.4	160.9
1	1.1	23.6	46.1	68.6	91.1	113.6	136.1	158.6

4.1.2 OUTER ITERATION 2: AXIAL AND RADIAL POWER DISTRIBUTION

In the second approach (*outer iteration 2*) to obtain representative fuel compositions of an equilibrium core, each of the 10 axial zones was divided into 3 radial zones. The axial zones remained equal in volume, but the radial zones differed in volume: each inner and outer region contained $1/8^{th}$ of the zone volume, and the middle zone contained $6/8^{th}$ of the zone volume. The fuel compositions obtained in outer iteration 1 were

used in the PB-FHR-Mk1 full core model to obtain the power profile according to these zones (see Figure 21 for the ring-wise axial power profiles from outer iteration 1).

The iterations in this approach followed the same scheme that was used for outer iteration 1. Additionally, the following conditions were applied to obtain the fuel compositions in the individual axial and radial zones during the eight passes:

1. A fuel pebble travels upwards through the axial zones within one radial zone: the fuel pebble does not switch radial zones within a pass.
2. The power during a burnup step in a certain radial zone (within an axial zone) accounts for the axial and radial power distributions.
3. The fuel compositions of the three radial zones of the top axial zone (axial zone 10) were averaged after each pass according to their volumes; these fuel compositions were used as the starting composition of *all* radial zones for the next pass.

Condition 1 seems reasonable because the pebbles tend not to mix between the zones, but rather, they travel straight upwards in the core.

Condition 2 assumes that fuel pebbles traveling through the inner radial zone experience greater power than those traveling through the outer radial zone (see Figure 23). Furthermore, the power is lower in the lowest and uppermost axial zones than in the middle zones. Consequently, fuel pebbles which have traveled through the inner radial zone accumulate more burnup compared to fuel pebbles that traveled through the outer radial zone.

Condition 3 was applied because it seemed reasonable and more feasible than specifying a particular travel history for each pebble. Every assumed travel history of a pebble (pass 1: inner radial zone; pass 2: middle radial zone; pass 3: outer radial zone; and so on) would be arbitrary. A different approach could randomly sample the radial zone of a pebble for each pass and determine the average results from multiple iterations. However, even this approach might not represent the actual refueling strategy that is used during the reactor operation.

The average fuel composition of each zone was calculated by averaging this zone's fuel compositions during the different passes. Core-average compositions for the iteration process were determined by averaging the fuel compositions of all zones considering their volume.

4.1.3 SENSITIVITY OF THE CORE-AVERAGE INVENTORY TO THE TEMPERATURE DURING DEPLETION

Besides the previously mentioned assumptions for the calculation of the core inventory, it is further noted that the above presented approach involves the depletion calculation of a core slice model with fixed material temperatures that correspond to average hot full-power conditions. Temperature distributions in the reactor as well as temperature variations during operation were not considered in these depletion calculations.

To understand the impact of the temperature during the slice depletion, a limited sensitivity study was performed in which the fuel temperature and the temperature in the graphite of the fuel pebbles were perturbed. The non-depletable fuel pebbles contained core-average fuel compositions as obtained from outer iteration 2. The temperatures were always perturbed for both the depletable surrogate fuel pebbles and the non-depletable fuel pebbles. The obtained burnup-dependent nuclide densities and the resulting core-average nuclide densities were compared between the calculations of the following conditions:

- Nominal depletion (reference): Average temperatures were applied for all materials.
- Fuel temperature perturbation by -200 K, -100 K, +100 K and +200 K.

- Graphite in fuel pebble temperature perturbation by -200 K, -100 K, +100 K, and +200 K.

Table 5 displays the relative differences of nuclide densities of important actinides and fission products obtained from the perturbed slice depletion compared to the nuclide densities from the reference depletion calculation. The maximum difference of the burnup-dependent nuclide densities and the difference of the resulting core-average fuel composition (determined using the approach detailed in the previous sections) are displayed.

When perturbing the fuel temperature, differences in the actinide densities during depletion of almost 7% were observed. The corresponding differences in the core-average composition were smaller with up to 4%. The impact of the fuel temperature perturbation was smaller for the fission products for which up to 4.5% difference was observed during depletion and a maximum difference of 2.5% was observed for the core-average composition. The impact of the perturbation of the graphite temperature in the fuel pebbles on the nuclide densities was larger for many investigated nuclides. The differences for some actinides were up to 15%, and the differences for some fission products reached values up to 10%.

This limited sensitivity study shows that temperature is clearly an important effect for the calculation of the core inventory, as also previously determined from the analyses of the PBMR-400 [Skutnik & Wieselquist, 2021]. While in the present study, we assumed average temperatures in the depletion calculations for the generation of the core inventory, capabilities will be developed in SCALE to consider that the pebbles experience time-dependent temperature effects while traveling through the reactor core.

4.1.4 DISCUSSION OF APPROACH

Tables 6 and 7 present the results of outer iterations 1 and 2, respectively. For each inner iteration *i*, the final depletion time, the discharge burnup, the k_{eff} of the initial neutron transport calculation, and the determined core-average nuclide densities (N_D) are displayed. In case of the burnup, the relative deviation from the target discharge burnup of 180 GWd/MTIHM is displayed. For k_{eff} and the densities, the difference from the previous iteration's value is shown. The statistical uncertainty of all displayed k_{eff} values is below 20 pcm. Although only the densities of ^{235}U and ^{239}Pu are displayed, other relevant nuclides, including fission products, were analyzed.

For the inner iterations of outer iteration 1, convergence was reached after 8 iterations, although 7 iterations would have also been sufficient. The relative difference between the densities fell below 0.5%, the k_{eff} difference was within the statistical uncertainty of k_{eff}, and the difference to the target burnup was less than 0.05%. For the inner iterations of outer iteration 2, convergence was reached after 9 iterations. The relative difference between the densities fell below 0.6%, the k_{eff} difference was within the statistical uncertainty of k_{eff}, and the difference to the target burnup was less than 0.25%.

The fuel compositions obtained from both outer iterations were applied in the PB-FHR-Mk1 full core model to obtain the axial and radial power profiles. A comparison calculation was also performed for a full core model with fresh fuel in all fuel pebbles. Figures 21 and 22 show that the difference between the power profiles of the equilibrium core models is very small, with a relative difference of 6% in the lowermost zone. The difference of these profiles compared to the profile obtained for the fresh core is, however, clearly visible. The axial power peak of the fresh core is much higher than that of the other profiles. This is the result of the traveling path of the fuel pebbles from the bottom to the top of the core which is considered during generation of the fuel composition for the equilibrium core. The burnup of all fuel pebbles (independent of the number of the pass) increases while traveling to the top of the core, whereas the generated power decreases with increasing burnup. Consequently, the average burnup of the pebbles increases with increasing core height, and the average generated power in these zones decreases. The power dip at the bottom of the core shows that significant power is generated in the inlet region to the main core (see Figure 16).

Table 5. Nuclide density differences due to temperature perturbation: maximum observed difference of burnup-dependent nuclide densities and difference of the resulting core-average fuel composition.

Nuclide	Fuel temp. perturbation		Graphite temp. perturbation	
	maximum abs. diff. during depletion	maximum abs. diff. core-average inventory	maximum abs. diff. during depletion	maximum abs. diff. core-average inventory
^{235}U	0.94%	0.91%	2.80%	0.87%
^{238}U	0.47%	0.17%	0.06%	0.00%
^{239}Pu	5.65%	4.04%	5.53%	3.72%
^{240}Pu	6.80%	3.98%	3.84%	1.54%
^{241}Pu	5.48%	3.21%	9.36%	2.34%
^{242}Pu	5.43%	1.98%	11.37%	4.61%
^{241}Am	5.64%	2.49%	9.14%	1.84%
^{244}Cm	6.95%	2.10%	14.28%	8.74%
^{245}Cm	6.05%	2.86%	14.45%	11.78%
^{85}Kr	0.59%	0.53%	1.63%	0.74%
^{90}Sr	0.54%	0.56%	1.63%	0.81%
^{110m}Ag	4.54%	1.01%	2.66%	1.81%
^{131}I	2.93%	1.77%	1.40%	0.38%
^{135}Xe	4.04%	2.46%	6.82%	5.35%
^{134}Cs	2.08%	1.32%	2.99%	0.86%
^{137}Cs	1.23%	0.25%	1.49%	0.45%
^{148}Nd	1.18%	0.29%	1.58%	0.50%
^{149}Sm	3.23%	2.26%	7.50%	5.89%
^{151}Sm	3.01%	1.66%	5.80%	4.55%
^{153}Eu	1.61%	0.19%	2.06%	0.37%
^{154}Eu	1.92%	0.62%	3.22%	1.19%
^{155}Eu	1.53%	1.44%	9.37%	8.51%
^{154}Gd	1.27%	2.29%	3.09%	1.26%
^{155}Gd	2.52%	0.32%	2.43%	0.89%

Very small differences were observed when comparing the inventory of the equilibrium core for the two outer iterations. The relative differences of the most important uranium and plutonium isotopes were below 1%. The relative differences of relevant fission and decay products were below 2% for the most abundant isotopes, and it was only slightly greater for nuclides with smaller nuclide densities (e.g., ^{135}Xe with a density of about ~4.5E-8 atoms/b-cm and a difference of ~3.6%). A few exceptions of very small densities showed larger differences (e.g., ^{155}Gd, with a density of ~3.0E-9 atoms/b-cm and a difference of ~9.5%).

It is possible to continue with another outer iteration based on the power profile obtained from outer iteration 2. However, given the small differences between the obtained power profiles from outer iterations 1 and 2, this was not pursued. It would also be possible to improve the approach further by reducing some of the chosen approximations that were detailed above. For example, it would be possible to adjust the temperatures in the 2D slice model during depletion to follow a temperature distribution according to the location of the pebble in the core (SCALE supports temperature perturbation during depletion). Similarly, it would be possible to consider different moderator-to-fuel ratios in the inlet and outlet area of the core by performing density perturbations of the inner and outer reflector during depletion. However, given the results of the temperature sensitivity study above and the significant modeling, computation and post-processing effort, this was not pursued. The surrogate fuel pebbles in the 2D slice model were exposed to representative conditions in the reactor during depletion through the application of average material temperatures, through consideration of radial leakage, through a realistic moderator-to-fuel ratio, and through depleted fuel in adjacent fuel pebbles. These conditions provided a realistic "average" neutron flux spectrum environment during depletion and were considered sufficient for the purpose of this study.

Although the applied approaches resulted in only rough approximations of fuel compositions during reactor operation, the results from outer iteration 2 were considered sufficient for these studies. The chosen iterative approach converged to a representative state from which the obtained inventory and the power distributions can be used with MELCOR for the analysis of severe accident scenarios.

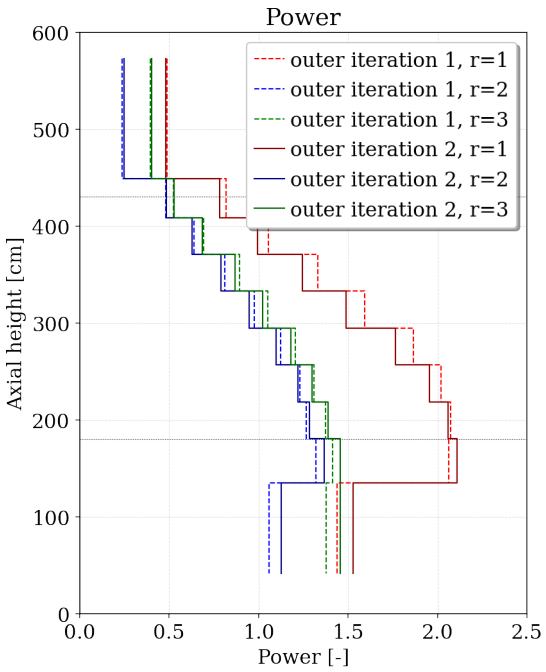

Figure 21. Ring-wise power profiles. See Figure 17 the boundaries of radial zones r=1 (inner), r=2 (middle), and r=3 (outer).

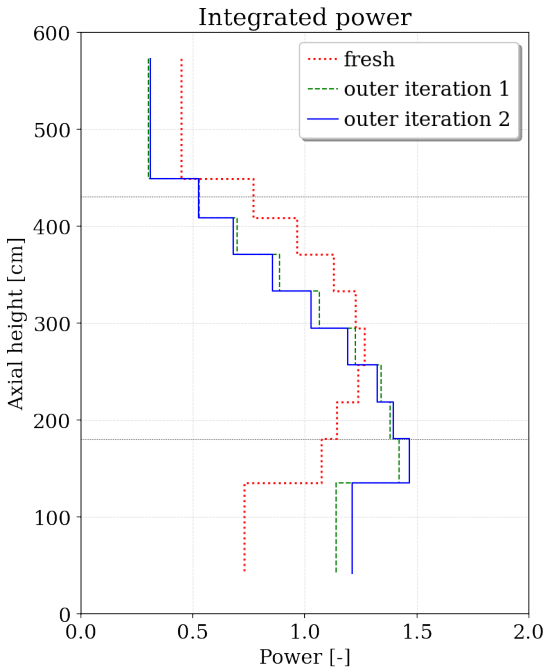

Figure 22. Axial power profile.

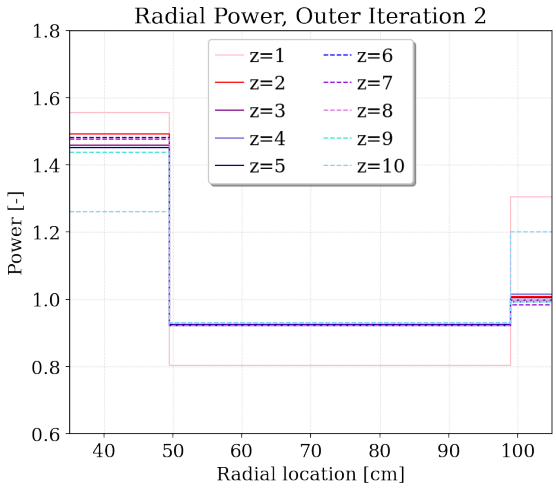

Figure 23. Radial power profiles. See Figure 17 for the location of the axial zones.

Table 6. Slice depletion calculation iterations of outer iteration 1 (constant power)

i	t_{final} (days)	bu_{final} (GWd/tHM)	$\frac{bu_{final}}{180\ GWd/tHM} - 1$	k_{eff}	$k_i - k_{i-1}$ (pcm)	N_D ^{235}U ($atoms/b-cm$)	$\frac{N_{D_i}}{N_{D_{i-1}}} - 1$	N_D ^{239}Pu ($atoms/b-cm$)	$\frac{N_{D_i}}{N_{D_{i-1}}} - 1$
0	540.54	144.56	-19.69%	1.32689	–	2.454E-03	–	2.063E-04	–
1	673.08	194.90	8.28%	1.03112	-29577	2.257E-03	-8.00%	2.147E-04	4.10%
2	621.63	187.44	4.13%	1.00464	-2648	2.273E-03	0.71%	2.104E-04	-2.02%
3	596.95	182.68	1.49%	1.00680	216	2.294E-03	0.91%	2.098E-04	-0.27%
4	588.21	180.39	0.22%	1.00954	274	2.304E-03	0.44%	2.102E-04	0.16%
5	586.94	180.15	0.08%	1.01046	92	2.307E-03	0.14%	2.114E-04	0.59%
6	586.45	180.01	0.00%	1.01120	74	2.314E-03	0.27%	2.123E-04	0.40%
7	586.43	179.84	-0.09%	1.01128	8	2.315E-03	0.04%	2.126E-04	0.18%
8	586.95	179.95	-0.03%	1.01126	-2	2.316E-03	0.06%	2.127E-04	0.05%

Table 7. Slice depletion calculation iterations using outer iteration 2 (axial/radial power profile)

i	t_{final} (days)	bu_{final} (GWd/tHM)	$\frac{bu_{final}}{180\ GWd/tHM} - 1$	k_{eff}	$k_i - k_{i-1}$ (pcm)	N_D ^{235}U ($atoms/b-cm$)	$\frac{N_{D_i}}{N_{D_{i-1}}} - 1$	N_D ^{239}Pu ($atoms/b-cm$)	$\frac{N_{D_i}}{N_{D_{i-1}}} - 1$
0	540.54	144.56	-19.69%	1.32689	–	2.454E-03	–	2.0881E-04	–
1	673.08	194.18	7.88%	1.03206	-29483	2.257E-03	-8.20%	2.1643E-04	3.65%
2	623.93	187.83	4.35%	1.00585	-2621	2.273E-03	0.93%	2.1384E-04	-1.20%
3	597.91	182.83	1.57%	1.00772	187	2.294E-03	0.96%	2.1432E-04	0.22%
4	588.67	180.46	0.26%	1.00991	219	2.304E-03	0.61%	2.1516E-04	0.39%
5	587.16	179.74	-0.14%	1.01122	131	2.307E-03	0.06%	2.1491E-04	-0.11%
6	588.01	179.62	-0.21%	1.01218	96	2.314E-03	0.03%	2.1403E-04	-0.41%
7	589.24	180.11	0.06%	1.01256	38	2.315E-03	-0.06%	2.1468E-04	0.31%
8	588.87	179.76	-0.13%	1.01178	-78	2.316E-03	-0.10%	2.1390E-04	-0.36%
9	589.66	180.40	0.22%	1.01168	-10	2.316E-03	0.01%	2.1432E-04	0.20%

4.2 NEUTRON FLUX DISTRIBUTION OF THE EQUILIBRIUM CORE

Figure 24 shows the normalized flux per lethargy in four different radial regions at the axial center of the core. The fast neutron flux is naturally the largest in the fuel pebble region, which is where the neutrons are born. As mentioned in the introduction, the ragged structure in the fast region is caused by elastic scattering with the salt components. All regions show a significant thermal peak, but the thermal flux is the largest in the inner graphite reflector.

Figures 25 to 29 present the neutron flux per fission neutron divided by the mesh voxel volume from a full core calculation with a mesh-tally covering the entire the core.

Figure 25 shows the total neutron flux in a horizontal plane through the center of the core. Due to radial leakage, the largest flux can be found in the radial center of the core. Figures 26 and 27 show the fast and thermal flux distribution in the full core, respectively. As a result of axial and radial leakage and the axial burnup distribution, the fast flux shows a maximum in the lower inner fuel region, which is consistent with the obtained power profiles (Figure 21). The thermal flux shows the maximum values in the inner reflector of the core axially, as seen in the region where the highest fast flux and the maximum power are also observed.

Figure 28 shows the radial profile of the fast and thermal fluxes. The fast flux peak towards the inner fuel region is clearly visible. In addition to the large thermal peak in the inner reflector region, the thermal flux also shows a smaller reflector peak in the graphite pebble region. Figure 29 shows the axial profile of the fast and thermal fluxes in the middle of the fuel pebble region. The thermal peak shows small peaks at about 110 and 500 cm, which result from the additional moderation in the inlet/outlet regions (changing moderator-to-fuel ratio in these regions). The fast flux shows that the peak shifted in the lower region, just as in the power profile.

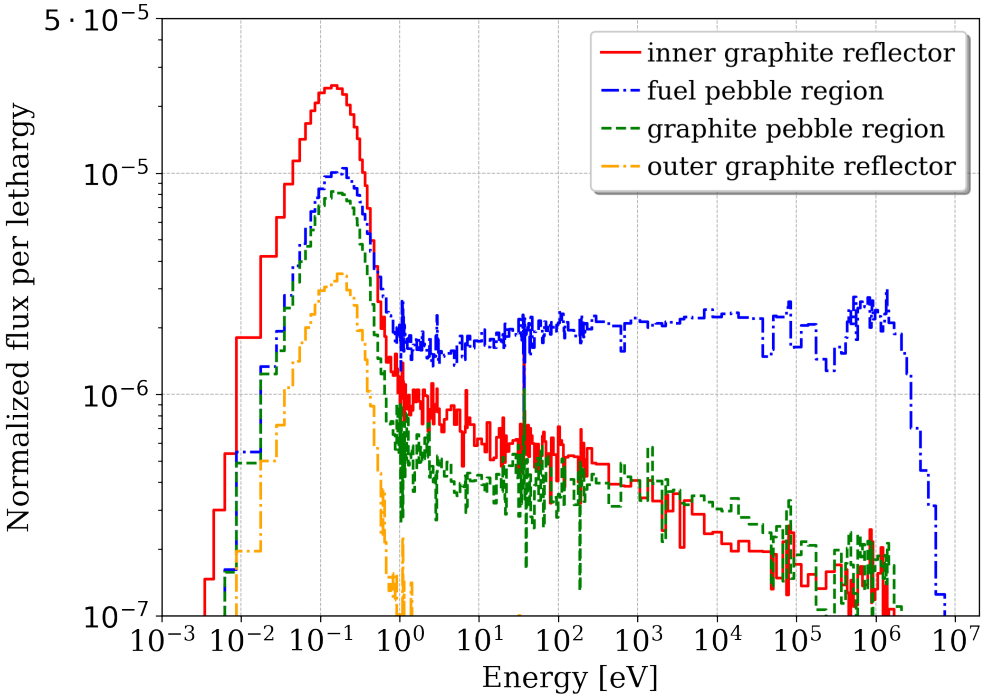

Figure 24. Normalized energy-dependent flux in different regions of the equilibrium core at the axial center.

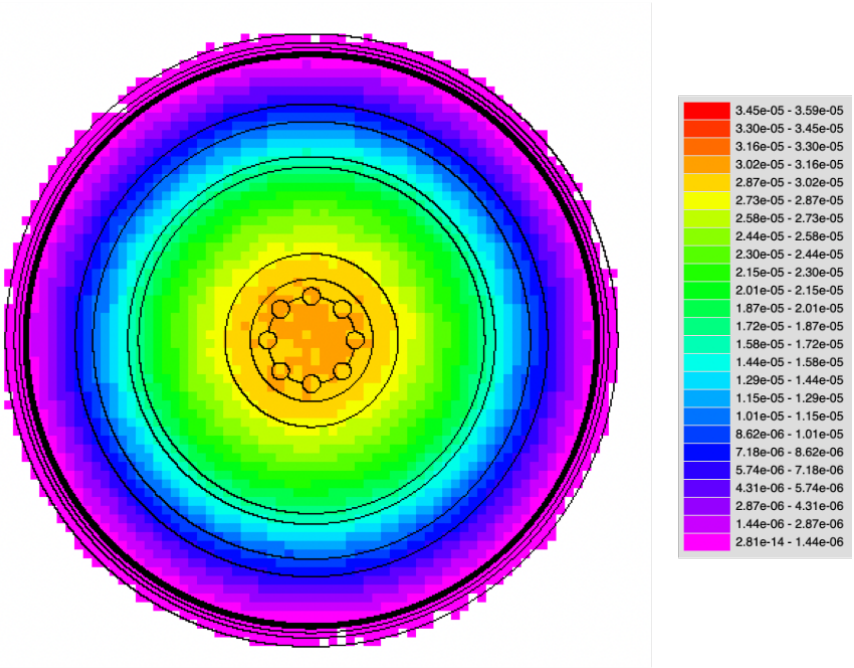

Figure 25. Total normalized neutron flux at the axial center of the equilibrium core.

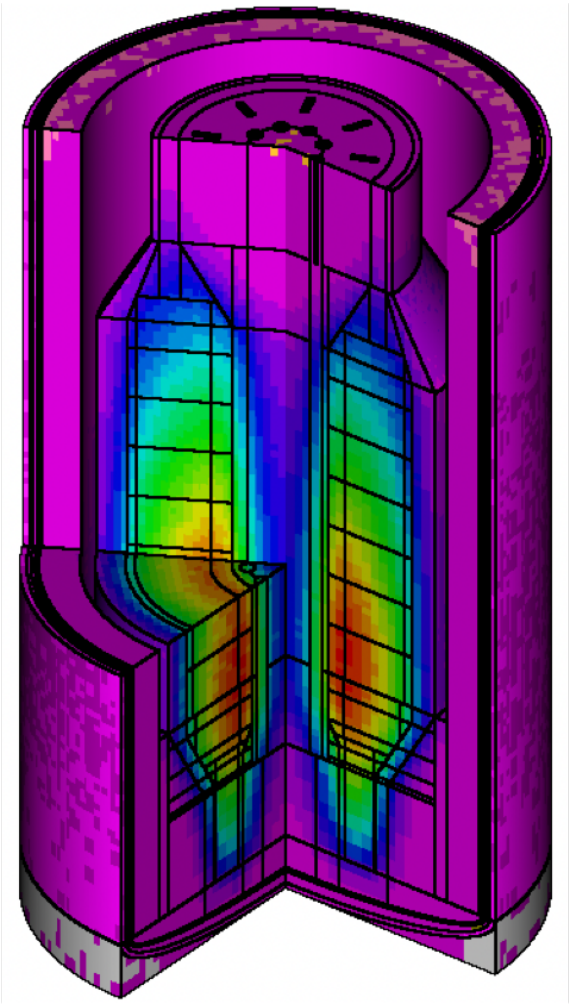

Figure 26. Normalized fast neutron flux (E > 0.615 eV) in the equilibrium core (see Fig. 25 for color scale).

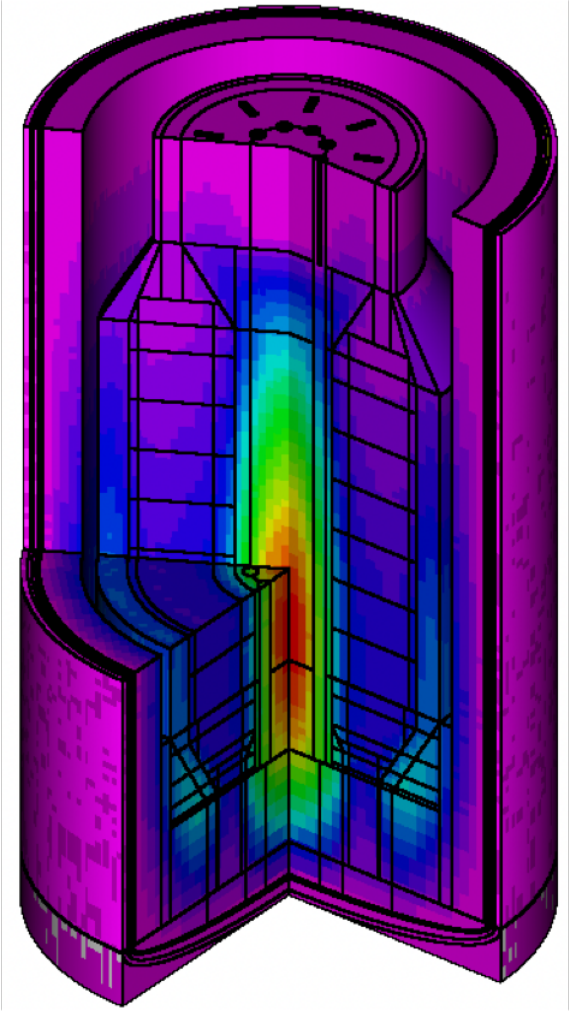

Figure 27. Normalized thermal neutron flux (E < 0.615 eV) in the equilibrium core (see Fig. 25 for color scale).

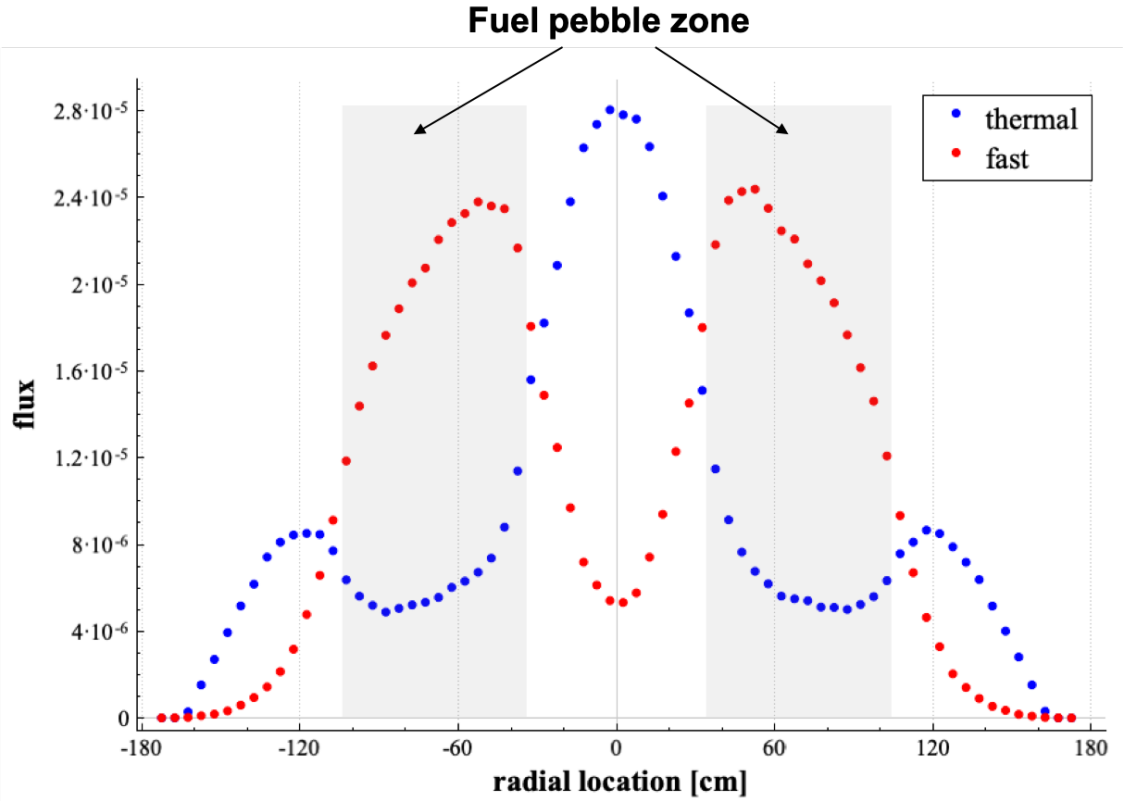

Figure 28. Normalized radial flux at the axial center of the equilibrium core.

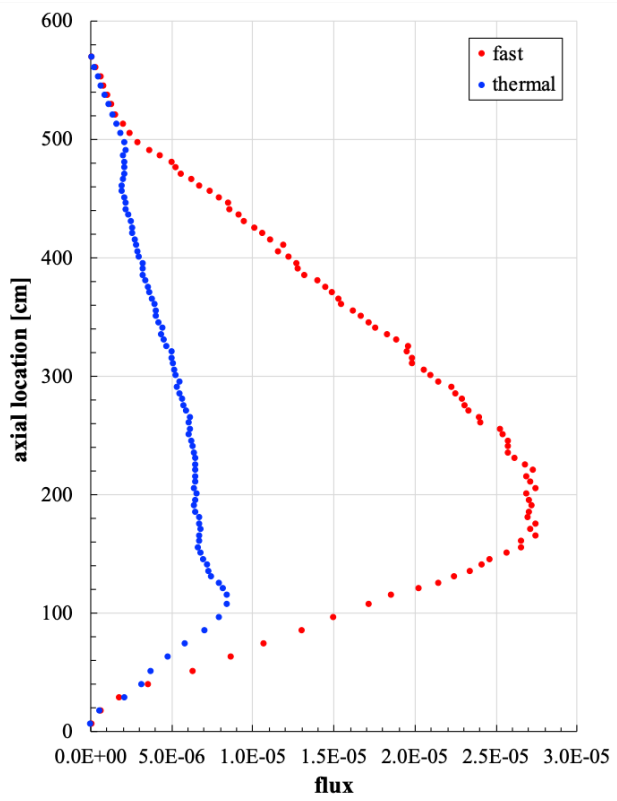

Figure 29. Normalized axial flux in the middle of the fuel pebble region of the equilibrium core.

4.3 DECAY HEAT OF THE EQUILIBRIUM CORE

In addition to the core inventory and power distribution, information on decay heat is required to simulate accident scenarios with MELCOR. As mentioned in the introduction, the analysis of the equilibrium core is the limiting case, as it has the highest expected decay heat compared to a startup core or at any state in which the startup core is slowly moving towards an equilibrium state after the reactor first started operation. This is because decay heat is increasing with burnup, and the highest core-average burnup can be found in the equilibrium state, as compared to a start-up core or a core with a short operation history which has a large number of fresh fuel pebbles and graphite pebbles in the fuel region.

The decay heat of the equilibrium core is presented in Figure 30 in terms of % of full power for 10 days after shutdown. The decay heat immediately after shutdown is ~5.6% of the reactor power, mainly as a result of the fission products. Figures 32 and 33 show the relative contributions of the top 10 fission products and the top 10 actinides to the decay heat during the first 10 days of decay. Figure 31 compares the decay heat of the PB-FHR-Mk1 with the decay heat of a pressurized water reactor (PWR) at 60 GWd/MTIHM burnup. The initial decay heat of the PWR is higher with ~6.5% of the PWR reactor power than that of the PB-FHR-Mk1.

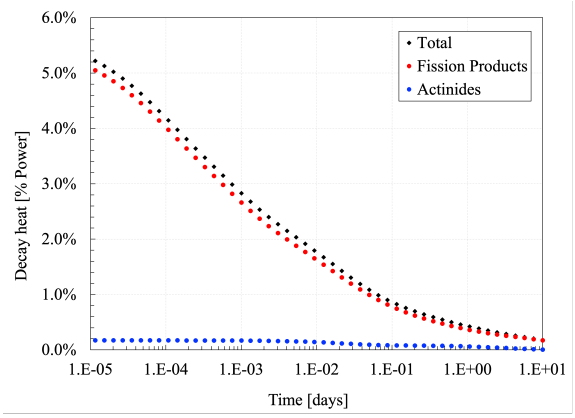

Figure 30. Decay heat of the equilibrium core.

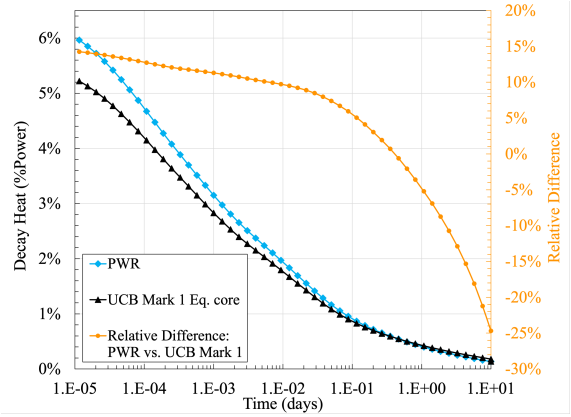

Figure 31. Comparison between PWR and FHR.

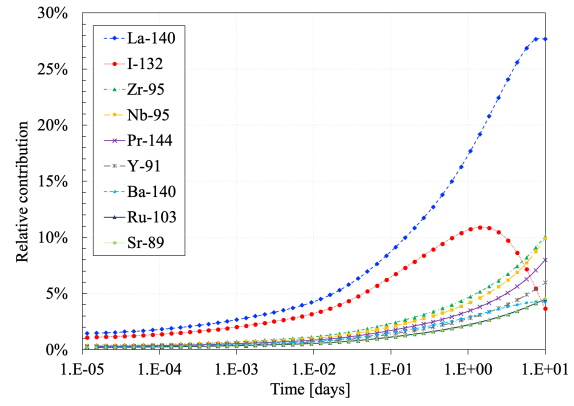

Figure 32. Relative contribution of fission products to decay heat.

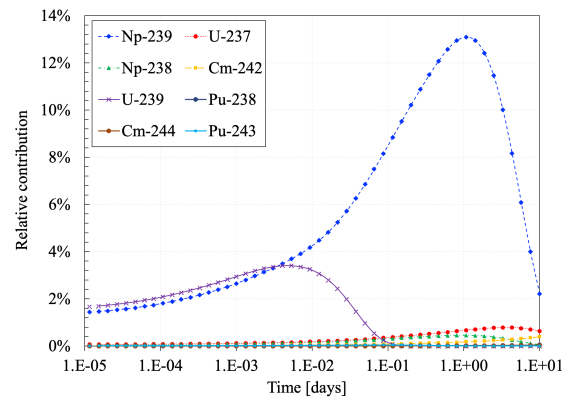

Figure 33. Relative contribution of actinides to decay heat.

4.4 ISOTHERMAL TEMPERATURE COEFFICIENTS OF THE EQUILIBRIUM CORE

To estimate the isothermal temperature coefficients, criticality calculations were performed while varying material temperatures over a range of several hundred Kelvin. Temperatures were assumed to be constant within the selected materials. The temperature coefficients were obtained as the gradients of the fitted curves for the calculated reactivities $\rho(T)$ as a function of temperature T. Is it explicitly noted here that density changes due to temperature changes were not accounted for in this analysis.

To allow for comparison with the results obtained by Cisneros [Cisneros, 2013], the temperatures were varied in the components listed in Table 8. For reference, this table provides the nominal temperatures of the materials at hot full-power (HFP).

Table 8. Components for which temperature coefficients were determined

Component	Description	Nominal temperature at HFP
Fuel	All fuel kernels in all fuel pebbles	1003 K
Salt coolant	Salt coolant around fuel pebbles (but not around graphite pebbles)	923 K
Graphite moderator	All carbonaceous materials in the fuel pebbles	973/983 K
Inner reflector	All materials within the inner reflector zone (i.e., graphite and the mixture of graphite and coolant)	873 K
Outer reflector	All materials in the outer reflector zone, all graphite pebbles, and the salt around the graphite pebbles	973 K

The reactivity of the salt coolant shows a linear behavior as a function of temperature (Figure 34). The isothermal temperature coefficient for this component could therefore be determined through linear fitting.

The reactivities obtained when varying the fuel temperature behave approximately in a linear manner. However, within certain smaller temperature intervals, the gradient varies slightly. The reactivities of the moderator and the inner and outer reflector structures clearly show a nonlinear behavior (Figure 35). Therefore, these reactivities were fit with polynomials of 2nd order:

$$\rho(T) = a + bT + cT^2 \tag{1}$$

The fitted parameters for all reactivities are presented in Table 9. If desired, the temperature coefficients can be converted from [1/K] to [$/K] by using the delayed neutron fraction for this system, which was determined as $\beta_{\text{eff}} = -0.00541 \pm 0.00020$. The fitted reactivity curve when varying the moderator temperature seems not to follow a 2nd order polynomial, but a polynomial of higher order. However, when using 3rd and 4th order polynomials for fitting, the uncertainty of the fitted parameters dramatically increase and such that no estimate on the gradient at certain temperatures can be made. To obtain a rough idea of the temperature feedback from the moderator, a 2nd order fit was considered sufficient.

The temperature coefficients at certain temperature points can be determined by evaluating the gradient of the obtained fitted curves by evaluating the derivatives of Eq. (1) at these temperature points of interest. For example, to compare the obtained temperature coefficients with the results from Cisneros, the gradients of the obtained temperature coefficients were determined *at the nominal HFP temperatures* as listed in Table 8, and then they were compared to Cisneros's results (Table 10). In case of the linear fit for salt reactivity, the gradient is constant over the entire temperature range; for the other coefficients, the presented values are the gradients evaluated at the specified temperature points. Cisneros's results and the SCALE results agree well

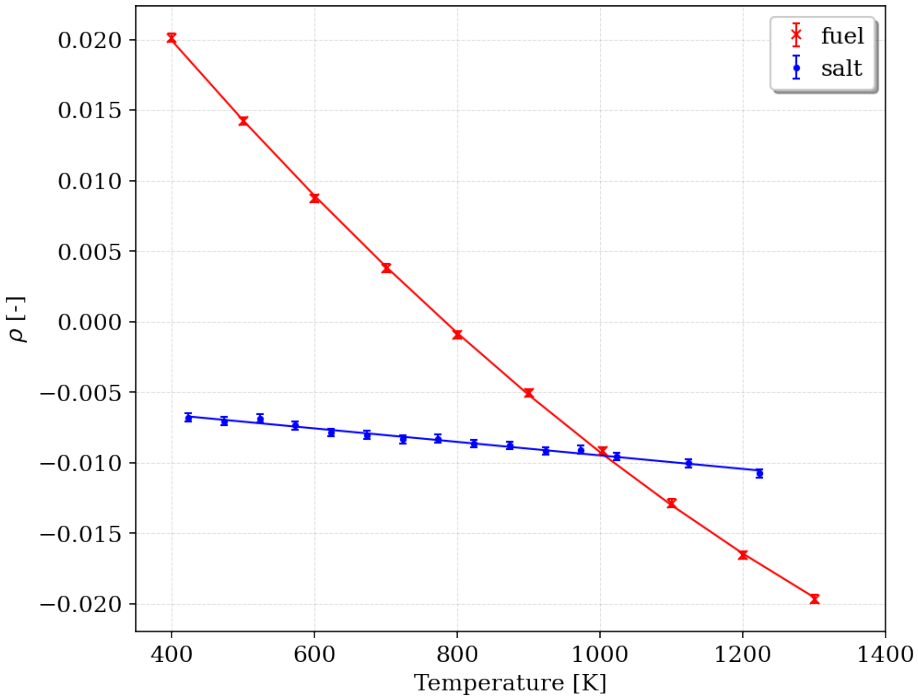

Figure 34. Temperature feedback of the fuel and the salt around the fuel pebbles: calculated reactivities ρ (including 2σ statistical error bars) and fitted curves.

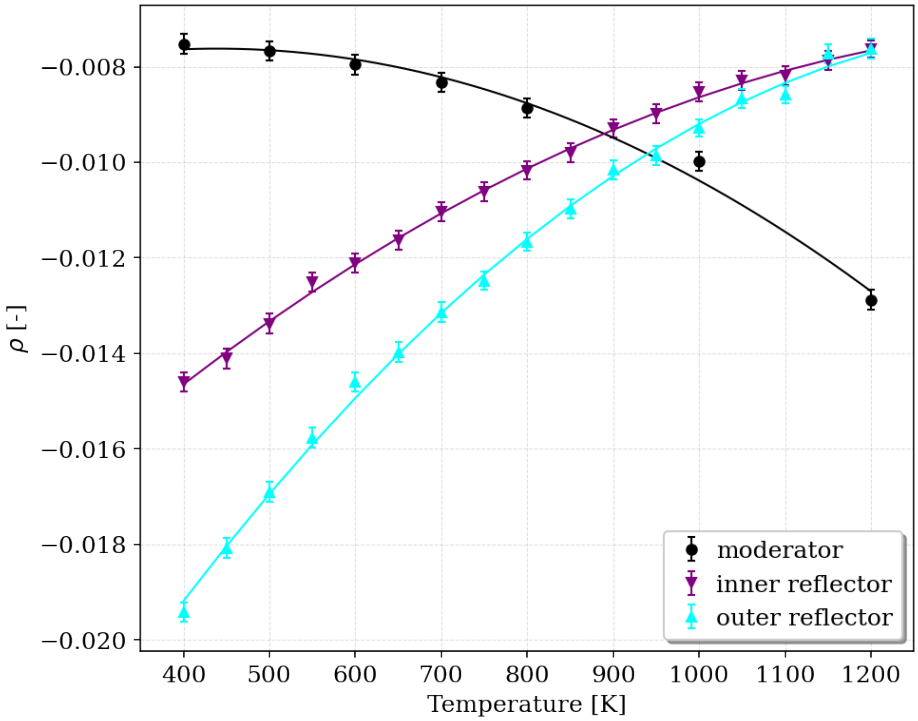

Figure 35. Temperature feedback of the graphite moderator in the fuel pebbles, the inner reflector, and the outer reflector: calculated reactivities ρ (including 2σ statistical error bars) and fitted curves.

for the fuel temperature reactivity coefficient. All other reactivity coefficients show large differences, although the general trend in terms of positive vs. negative reactivities is identical. These differences can be caused by differences in modeling choices. A cause of the differences in the other coefficients could be differences in the fuel composition. The models contain different fuel compositions in a different choice of axial and radial zones. The fuel compositions were obtained from different approaches to model an equilibrium state and cause differences in spectral conditions. The use of different nuclear data libraries can also be a contributor to observed differences.

Negative values were obtained for the fuel, salt coolant, and graphite moderator temperature coefficients. In contrast, positive temperature coefficients were obtained for the inner and outer reflectors. Since these reflector structures mainly consist of graphite, the reactivity in these components is mainly influenced by the moderating effect of graphite. When comparing graphite's elastic scattering cross section at different temperatures (Figure 36), it is observed that the cross section increases with increasing temperature. This indicates that graphite has an increasing moderating effect with increasing temperatures, thus resulting in a positive temperature reactivity coefficient.

Table 9. Parameters for the fitted temperature reactivity curves following Eq. (1)

Component	a [-]	b $\left[\frac{1}{K}\right]$	c $\left[\frac{1}{K^2}\right]$
Fuel	4.577E-02 ± 5.306E-04	-7.099E-05 ± 1.355E-06	1.595E-08 ± 7.934E-10
Salt coolant	-4.699E-03 ± 1.506E-04	-4.785E-06 ± 1.855E-07	
Graphite moderator	-9.309E-03 ± 8.865E-04	7.698E-06 ± 2.396E-06	-8.771E-09 ± 1.482E-09
Inner reflector	-2.121E-02 ± 2.404E-04	1.896E-05 ± 6.337E-07	-6.387E-09 ± 3.898E-10
Outer reflector	-3.046E-02 ± 4.811E-04	3.278E-05 ± 1.272E-06	-1.152E-08 ± 7.855E-10

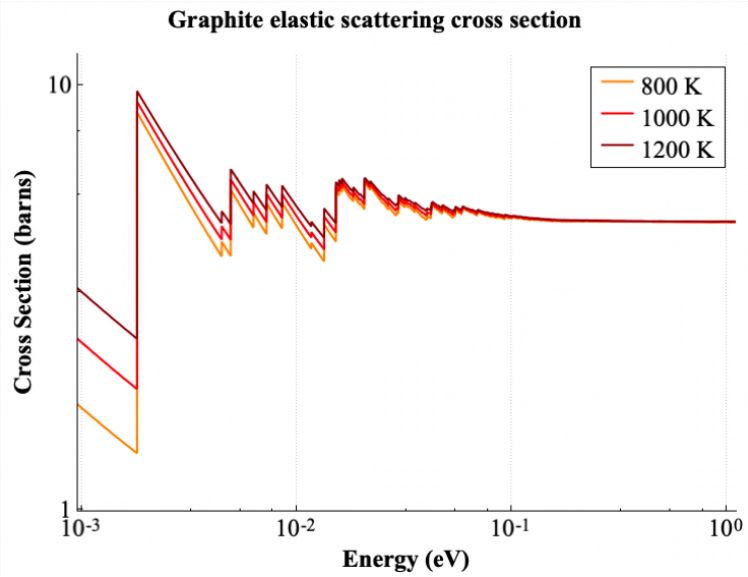

Figure 36. Elastic scattering cross section of graphite at different temperatures (CE, ENDF/B-VII.1).

4.5 SALT DENSITY EFFECT OF THE EQUILIBRIUM CORE

The temperature range for the FLiBe coolant during reactor operation is approximately 600–700°C (873–973 K). The melting temperature is 459°C (732 K), and it boils at over 1,430°C (1,703 K). If the salt

temperature is increasing, then the salt is expanding, and thus, the salt's density is decreasing. The density and temperature of FLiBe salt are correlated as follows [Romatoski & Hu, 2017]:

$$\rho = 10^{-3} \cdot \left(2413 - \frac{0.488}{T}\right), \tag{2}$$

with the density ρ in g/cm^3 and the temperature T in Kelvin.

In addition to studying the impact of salt temperature changes alone on the reactivity, the impact of temperature changes with concurrent change density changes according to Eq. 2 was considered. The reactivity coefficient for the salt's temperature was determined to be -0.48 pcm/K (Table 9), but a coefficient of -1.56 pcm/K was determined when the salt density is also considered. This value is in reasonable agreement with the coefficient of -1.8 pcm/K that Cisneros determined [Cisneros, 2013].

In addition to the temperature reactivity from Doppler broadening of resonances, the changes in salt density have a noticeable influence on reactivity. With increasing temperature and associated decreasing density, a negative reactivity contribution is obtained because there is less neutron interaction with the salt, causing a slightly harder neutron spectrum, and consequentially more leakage. However, a positive reactivity contribution is obtained through less absorption of neutrons from salt components. The negative contributions dominate such that the overall reactivity effect remains negative. Because the combined effect of temperature and density on the salt shows a much stronger gradient compared to the effect of temperature alone, it was concluded that the effect of reduced neutron interaction with the salt is more relevant than the effect of Doppler broadening. This is understandable, given that most of the salt components are 1/E absorbers, and the main resonances for which Doppler broadening is significant are in the scattering reactions in the fast energy range (e.g., Figure 2).

Table 10. Temperature reactivity coefficient comparison

Component	Temperature reactivity coefficient at HFP [pcm/K]	
	Cisneros [Cisneros, 2013]	ORNL
Fuel	-3.8	-3.90 ± 0.21
Salt coolant		-0.48 ± 0.02
Salt coolant[a]	-1.8	-1.56 ± 0.01
Graphite moderator	-0.7	-0.95 ± 0.38
Inner reflector	+0.9	+0.78 ± 0.09
Outer reflector	+0.9	+1.04 ± 0.20

[a] combined temperature and density effect

4.6 SENSITIVITY OF REACTIVITY COEFFICIENTS TO THE TEMPERATURE

The nominal full core model of the PB-FHR-Mk1 assumes constant temperatures in all materials. Instead of implementing temperature distributions, average temperatures are applied. For example, the temperature of the salt around the fuel pebbles is consistent with the average of the inlet and outlet salt temperature.

It is of interest to understand if the temperature reactivity coefficients determined for the nominal full core in the previous sections are sensitive to temperatures changes in the model. A sensitivity study was performed in which the temperatures in the salt surrounding the fuel pebbles and the fuel temperature were modified in 10 axial layers of the core.

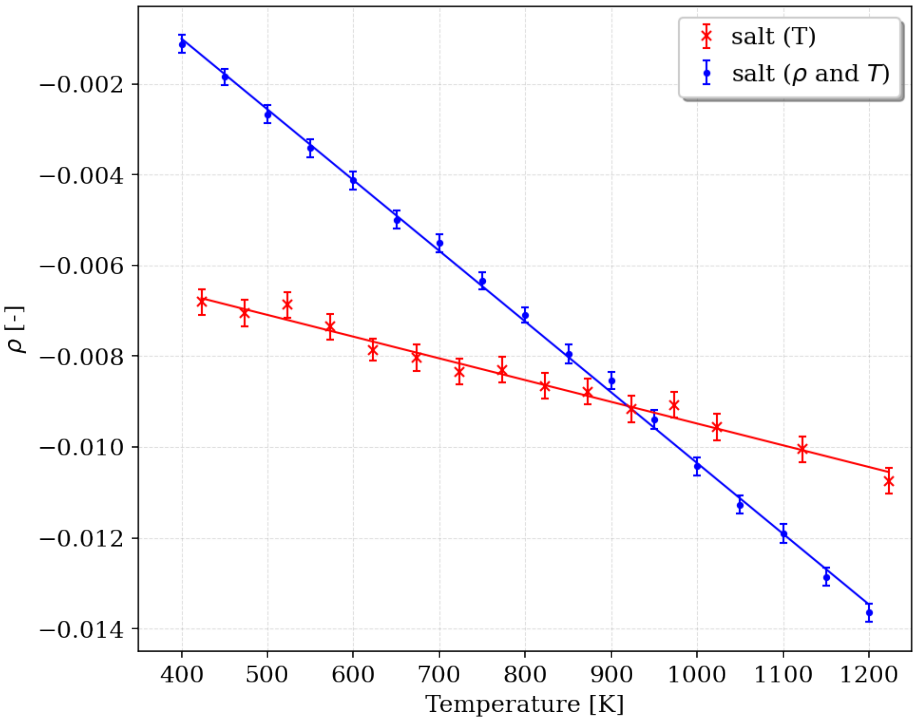

Figure 37. Combined temperature and density feedback of the salt around the fuel pebbles: calculated reactivities ρ (including 2σ statistical error bars), fitted curve, and a line indicating the salt temperature at HFP.

The fuel temperature feedback and the combined salt temperature and density feedback were calculated based on the following models:

- Nominal core: Average temperatures were applied for the fuel and the salt (1003 K and 923 K, respectively).
- Variation 1: The temperatures of the salt surrounding the fuel pebbles were modified in the 10 axial layers (see Figure 17) to linearly increase from 600°C at the core bottom (inlet) to 700°C at the top of the core (outlet); the salt densities were modified correspondingly using Eq. 2.
- Variation 2: The salt temperatures and densities were varied in the 10 axial zones as described in Variation 1. Additionally, the fuel temperature were modified in the 10 axial layers to approximately follow the axial temperature profile that was determined by MELCOR for the fuel pebbles. The resulting fuel temperatures varied between 969.4 K and 1034.0 K.

Figure 38 and Table 11 show that the influence of the applied modifications to the fuel and salt temperatures have a negligible influence on the gradients of the fitted curves. The maximum difference was obtained for the combined salt temperature and density effect which varied by 4%. In conclusion, the temperature feedback effects do not vary significantly when material temperatures distributions are applied instead of overage temperatures. It is noted that the sensitivity study here was focused on temperature variations during full power operation, and the study focused on only two materials.

Case	Fuel [pcm/K]	Relative difference	Salt [pcm/K]	Relative difference
nominal	-3.90 ± 0.21	(ref)	-1.56 ± 0.01	(ref)
V1	-3.89 ± 0.47	-0.1%	-1.59 ± 0.05	2.4%
V2	-3.93 ± 0.73	0.8%	-1.62 ± 0.03	4.0%

Table 11. Fuel temperature and combined salt temperature and density reactivity coefficient comparison

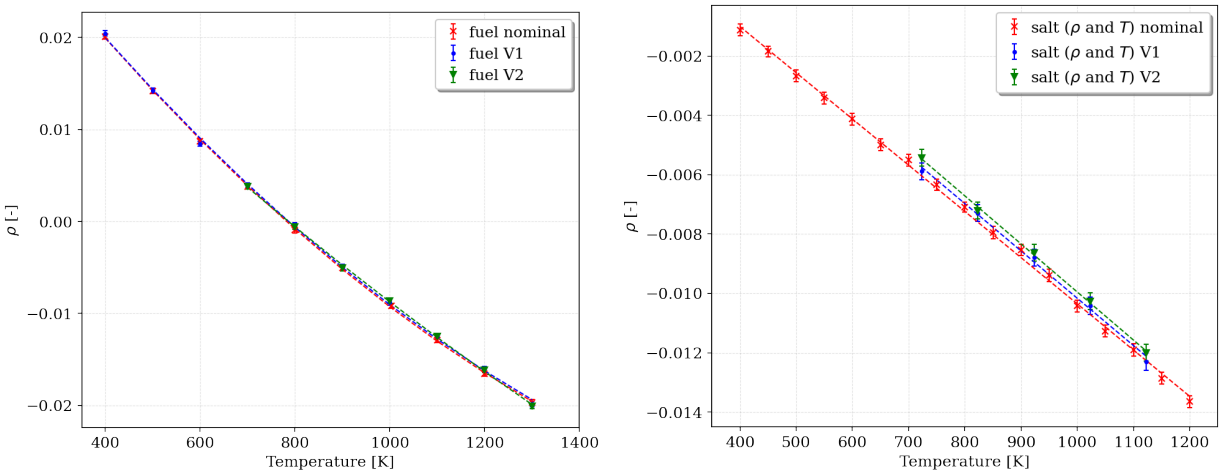

Figure 38. Fuel temperature (left) and combined salt temperature and density reactivity (right) ρ calculated using different temperature in the core.

5. TRITIUM ANALYSIS

5.1 BACKGROUND

Using FLiBe as a coolant leads FHRs to produce considerable quantities of tritium. When tritium production rates have reached an equilibrium, the rate per unit energy in an FHR is hundreds of times higher than the same rate in an LWR [Stempien et al., 2016]. The bulk of tritium production in an FHR is from neutron interactions with lithium and fluorine in the coolant, with the primary reactions of interest shown below.

$$
\begin{aligned}
&^{6}Li + n \rightarrow ^{4}He + ^{3}H \\
&^{7}Li + n \rightarrow ^{4}He + ^{3}H + n' \\
&^{19}F + n \rightarrow ^{17}O + ^{3}H
\end{aligned}
$$

Furthermore, neutron interactions with beryllium in the coolant produce ^{6}Li, partially or completely replenishing the initial ^{6}Li inventory that is depleted as the reactor starts up [Stempien et al., 2016]:

$$
^{9}Be + n \rightarrow ^{4}He + ^{6}Li + e^{-} + \bar{\nu}_{e}
$$

Previous work by Cisneros on FHR tritium production generation included development of an analytical model to estimate the tritium production rate [Cisneros, 2013]. In the following equation used by Cisneros, σ^{T} is the tritium production cross section, σ^{α} is the alpha particle production cross section, and σ^{abs} is the absorption cross section for a given nuclide:

$$
\dot{T}(t) = \phi\,\sigma^{T}_{Li-7}\,N_{Li-7} + \phi\,\sigma^{T}_{Li-6}\left(N^{0}_{Li-6}e^{-\frac{V_{core}}{V_{loop}}\,\phi\,\sigma^{abs}_{Li-6}\,t} + \frac{\phi\,\sigma^{\alpha}_{Be-9}N_{Be-9}}{\phi\,\sigma^{abs}_{Li-6}}\left(1 - e^{-\frac{V_{core}}{V_{loop}}\,\phi\,\sigma^{abs}_{Li-6}\,t}\right)\right). \tag{3}
$$

To assess SCALE's capability for modeling tritium production in FLiBe, TRITON was used to generate one-group cross sections for FLiBe activation which were then used by ORIGEN to deplete and activate the FLiBe coolant. The tritium production rates from this analysis were compared to those reported by Cisneros [Cisneros, 2013] and Stempien [Stempien et al., 2016] to demonstrate the applicability of the present models and modeling approach. Sampler was then used to conduct a parametric sweep over initial ^{7}Li enrichment and flux to demonstrate the impact of these parameters on the tritium production rate.

The PB-FHR-Mk1 design description specifies a total FLiBe volume of 46.82 m^{3}, with a total of 7.20 m^{2} in the core and the remainder in the reactor internals (3.38 m^{3}) and the primary loop (36.24 m^{3}) [Andreades et al., 2014]. During operation, tritium will be transferred from the coolant salt to surfaces in the system. The graphite surfaces, whether pebbles or reflector, serve as a sink for tritium, and metal surfaces such as heat exchangers provide additional sinks for tritium [Stempien et al., 2016]. The PB-FHR-Mk1 design includes a tritium filtering system in the form of cartridges containing 2-mm-diameter carbon balls located in the hot salt manifold of the heat exchanger. Salt flows through these cartridges, depositing tritium in the graphite prior to reaching the heat exchanger. This filtering system doubles the graphite surface area in the system and approximately halves the tritium content of the salt in the primary loop [Andreades et al., 2014].

5.2 TRITIUM PRODUCTION MODELING IN SCALE

To model tritium production in SCALE, the equilibrium PB-FHR-Mk1 core developed in Section 4.1 was used to generate one-group cross sections in FLiBe. A TRITON calculation of the core was performed in which only the coolant was depleted. This means that one-group cross sections for the coolant were calculated based only on the neutron flux in the coolant. Using these one-group cross sections, ORIGEN was applied for the FLiBe activation and depletion calculation. The calculated initial tritium production rate right after reactor start-up is 0.147 mol/equivalent full-power day (EFPD). As the initial ^{6}Li inventory was depleted during operation, the production rate fell to 0.021 mol/EFPD. As a result of the balance between ^{6}Li production from ^{9}Be and destruction due to neutron capture of ^{6}Li, tritium production arrives at an equilibrium after approximately 10 years of full-power operation (Figure 39).

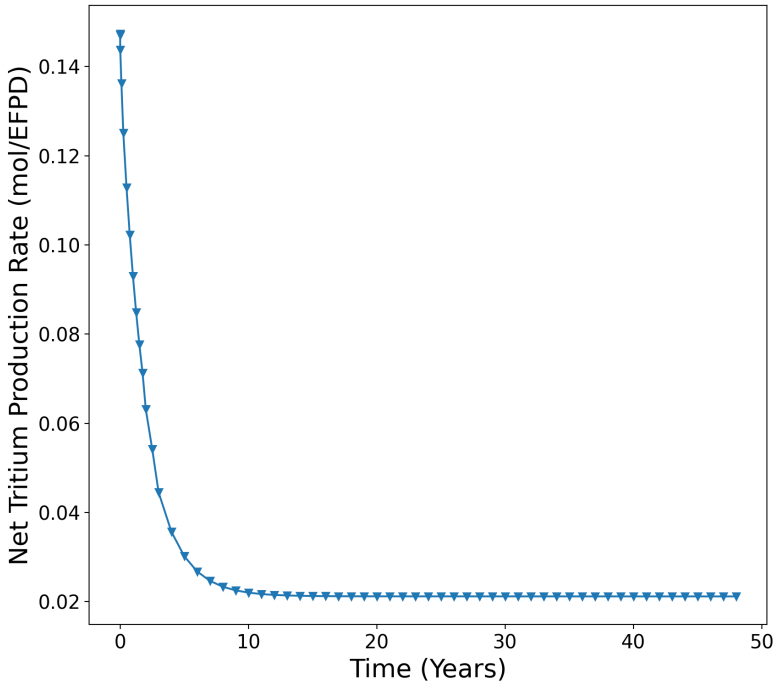

Figure 39. Tritium production rate over time as obtained with ORIGEN.

5.3 SAMPLER SENSITIVITY STUDY

After the ORIGEN model for tritium production was developed and the nominal calculation was performed, SCALE's Sampler sequence was used to conduct a sensitivity study examining the impact of (1) the flux and (2) the initial ^{7}Li enrichment on the tritium production rate. Sampler was used to sample these two input parameters using uniform distributions over the ranges shown in Table 12.

An average equilibrium tritium production rate of 0.021 mol/EFPD was obtained, with a minimum of 0.019 and a maximum of 0.023 mol/EFPD. In Figure 40, a large variation of the initial tritium production rates can be seen. This was driven by initial ^{7}Li enrichment and flux. While approaching the equilibrium production rate, the tritium production rates converge.

Figure 41 shows the individual sample results when the initial ^{7}Li enrichment and the flux are varied. Based on these figures, it can be concluded that the equilibrium tritium production rate is independent of the initial

^{7}Li enrichment and is strongly dependent on the flux, a result consistent with previous work [Stempien et al., 2016]. In contrast, the beginning of life (BOL) tritium production rate depends on the flux and the initial ^{7}Li enrichment. It is noted that the variation in tritium production rates at BOL is greater at lower initial lithium enrichment, indicating that the effect of neutron flux at BOL is greater when the initial ^{7}Li enrichment is lower, and as initial ^{7}Li enrichment increases, the impact of flux diminishes.

Table 12. Sampler sensitivity study parameters

Property	Minimum value	Maximum value
Flux $\left(\frac{n}{cm^2-s}\right)$	$3.528 \cdot 10^{14}$	$4.312 \cdot 10^{14}$
Initial ^{7}Li Enrichment (wt.%)	99.95	100

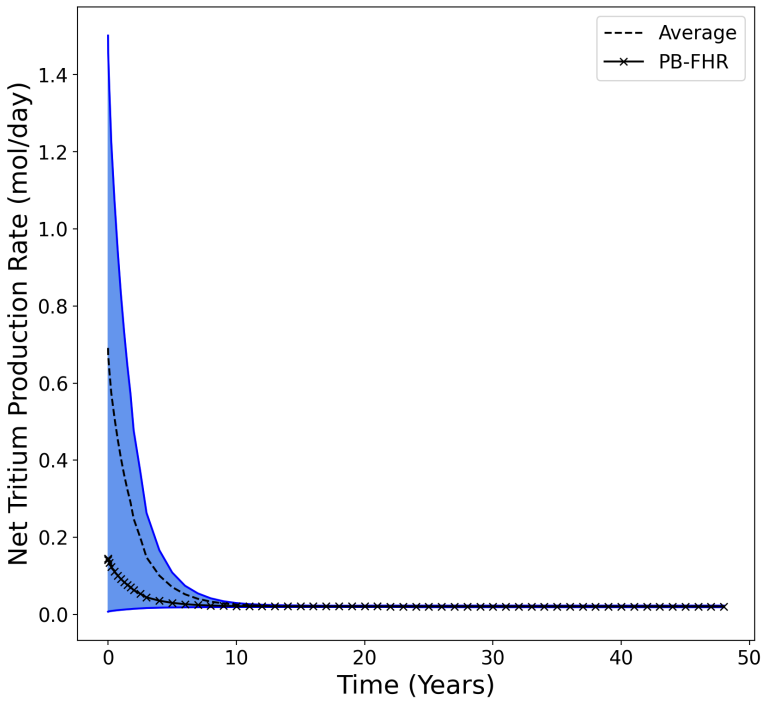

Figure 40. Calculated tritium production rates over time from the Sampler study.

Neglecting tritium losses from the salt, Figure 42 presents the tritium inventory over time. These values are extremely high and do not represent realistic estimates of the tritium inventory in the FLiBe. Rather, they represent an unmitigated tritium inventory that assumes once tritium is produced it only leaves the salt through radioactive decay.

5.4 CONCLUSIONS

Using the PB-FHR-Mk1 equilibrium core model as developed and discussed in Section 4, one-group FLiBe activation cross sections generated with TRITON were used to calculate tritium production rates with ORIGEN. An equilibrium tritium production rate of 0.021 mol/EFPD was obtained. The initial tritium

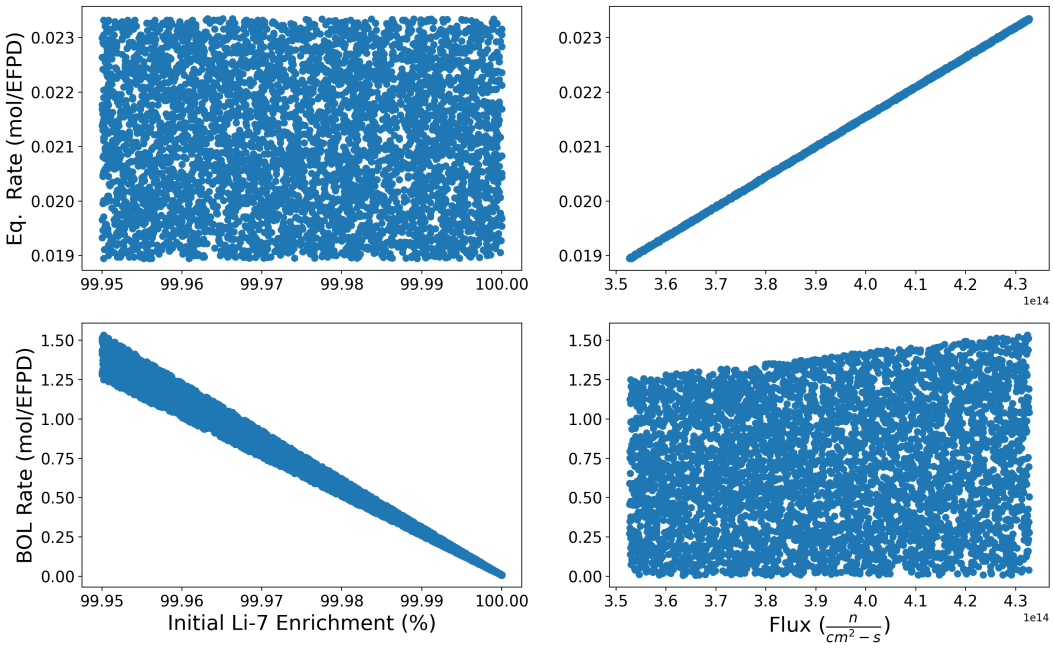

Figure 41. Dependence of the initial ^{7}Li enrichment (left) and the neutron flux (right) on the tritium production rates at BOL and at equilibrium.

production rate was 0.147 mol/EFPD as a result of a larger concentration of ^{6}Li at the BOL than at equilibrium, but as ^{6}Li was depleted and partially replenished from neutron reactions with ^{9}Be, tritium production rates approached equilibrium after approximately 10 years of full-power operation. Sensitivity calculations with Sampler revealed that the initial tritium production rate mainly depends on initial ^{7}Li enrichment, and the equilibrium tritium production rate is strongly dependent on the neutron flux.

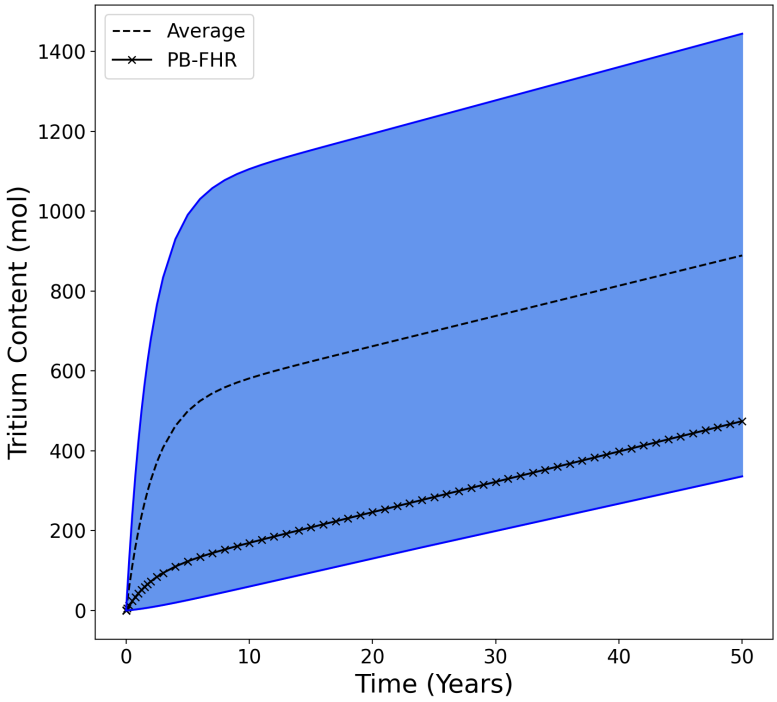

Figure 42. Calculated tritium inventory from the Sampler study.

6. XENON ANALYSIS

6.1 INTRODUCTION AND THEORY

During normal operation, reactors build up ^{135}Xe, a strong poison that affects some long-term transients. For example, the Japanese High Temperature Engineering Test Reactor demonstrated a re-criticality partially driven by ^{135}Xe build-up and decay following a loss of flow transient [Takamatsu et al., 2014]. ^{135}Xe is produced directly from fission and from the decay of ^{135}I. The evolution of ^{135}I and ^{135}Xe populations can be described by the following differential equations, where γ_n represents the fraction of fissions yielding isotope n, Σ_F is the whole-core macroscopic fission cross section, ϕ is the flux, σ_a^n is the microscopic absorption cross section for isotope n, and λ_n is the decay constant for isotope n:

$$\frac{dI}{dt} = \gamma_I \Sigma_F \phi - \lambda_I I \tag{4}$$

$$\frac{dX}{dt} = \gamma_X \Sigma_F \phi + \lambda_I I - \lambda_X X - \sigma_a^x X \phi. \tag{5}$$

During normal operation, reactors reach an equilibrium ^{135}Xe concentration, as production from fission and decay of ^{135}I are balanced with loss through decay and absorption. Following shutdown, the fission production and absorption destruction pathways are eliminated, but ^{135}Xe continues to build up from the decay of ^{135}I, which has a half-life of 6.58 hours. Decay of ^{135}Xe occurs with a half-life of 9.14 hours, which leads to an accumulation of ^{135}Xe until the decay of ^{135}I is outpaced by ^{135}Xe decay.

6.2 RESULTS

The equations dictating buildup and decay of ^{135}Xe can be solved analytically given a few simplifying assumptions and initial conditions. A simplified solution is presented here in which the flux is assumed to go to zero at a time of zero. This allows the fission production and absorption destruction pathways to be ignored, so equations can be solved considering only decay of ^{135}I and ^{135}Xe.

The steady-state concentrations of ^{135}I and ^{135}Xe were extracted from the equilibrium core model. The reactivity worth of the equilibrium ^{135}Xe concentration was -3,507 pcm. Dividing that by $\beta_{eff} = 0.00541$ yields a nominal ^{135}Xe reactivity of 6.48224\$. Thus, the xenon worth per unit ^{135}Xe can be calculated as follows:

$$\rho_{perXe} = -\frac{6.48224\$}{5.018 \cdot 10^{16} \frac{atoms}{cm^3}} = -1.29184 \cdot 10^{-16}\$ \cdot cm^3. \tag{6}$$

Multiplying the time-dependent ^{135}Xe concentration by ρ_{perXe} allows calculation of ^{135}Xe reactivity worth at any point in time. All calculations were conducted with Wolfram Mathematica, which is capable of providing symbolic solutions to differential equations, finding minima and maxima, and solving for the root systems of equations.

For the case in which fission power (and therefore flux) goes to zero, the differential equations simplify to the following:

$$\frac{dI}{dt} = -\lambda_I I \tag{7}$$

$$\frac{dX}{dt} = \lambda_I I - \lambda_X X. \tag{8}$$

If I_0 and X_0 are the steady-state ^{135}I and ^{135}Xe concentrations, respectively, then the solutions of Eqs. 7 and 8 are as follows:

$$I(t) = I_0 e^{-\lambda_I t} \tag{9}$$

$$X(t) = X_0 e^{-\lambda_X t} + \frac{\lambda_I I_0}{\lambda_I - \lambda_X}\left(e^{-\lambda_X t} - e^{-\lambda_I t}\right). \tag{10}$$

Multiplying Eq. (10) by ρ_{perXe} gives the ^{135}Xe reactivity at any time. The maximum reactivity from ^{135}Xe is −18.6334$, and it occurs 9.49 hours after shutdown. After 9.49 hours, the ^{135}Xe reactivity falls, ultimately falling below its steady-state value at a time of 34.67 hours, as seen in Fig 43. Eqs. (9) and (10) are consistent with those presented in *Introduction to Nuclear Engineering* by Lamarsh and Baratta [Lamarsh & Baratta, 2001].

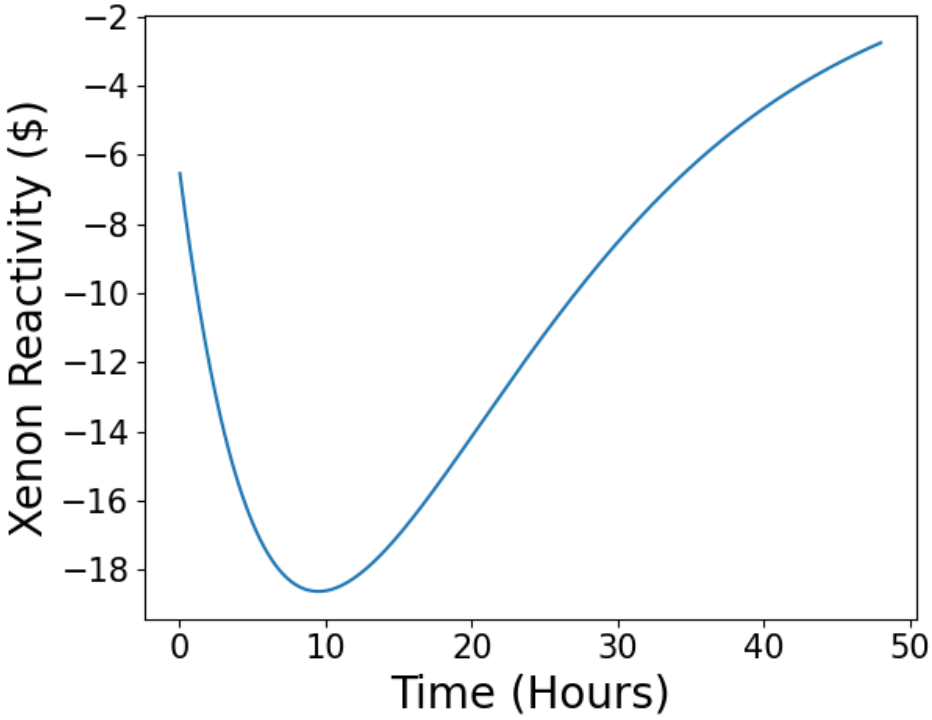

Figure 43. Calculated ^{135}Xe reactivity after shutdown.

6.3 CONCLUSIONS

Modeling the buildup and decay of ^{135}Xe is important for modeling long-term transients in reactors. For the PB-FHR-Mk1 with steady-state ^{135}I and ^{135}Xe concentrations calculated using SCALE, the maximum ^{135}Xe

reactivity worth is -18.6334\$, which occurs 9.49 hours after flux goes to zero. The ^{135}Xe reactivity falls below its steady-state value after 34.67 hours. The differential equations to produce these results were solved using Wolfram Mathematica and match those presented in Lamarsh and Barratta [Lamarsh & Baratta, 2001].

7. ORIGEN LIBRARY GENERATION

SCALE's ORIGAMI code enables rapid calculations of detailed isotopic compositions by using ORIGEN with pre-generated ORIGEN binary libraries. ORIGAMI is currently supporting typical UOX-based LWR assemblies, but further development to support non-traditional reactor systems with rapid evaluations of core inventories is planned. Because the parameterization of pre-generated ORIGEN libraries for LWR assemblies (e.g., for moderator density) might not be sufficient for systems such as the FHR, the spectral variations and their impact on the ORIGEN binary libraries, in particular the one-group cross sections on these libraries, must be understood.

Extensive studies have been performed for the PBMR-400 benchmark, a graphite-moderated pebble bed reactor with helium coolant [Skutnik & Wieselquist, 2021]. In this section, the dependence of one-group cross sections on the burnup and location in the equilibrium core is analyzed to determine if the conclusions drawn for the PBMR-400 benchmark are also applicable to the PB-FHR-Mk1. One-group removal cross sections for ^{235}U, ^{239}Pu, ^{240}Pu, and ^{241}Pu were studied.

7.1 BURNUP DEPENDENCE

Figure 44 shows the development of the one-group removal cross section as a function of burnup from the depletion of a slice of the PB-FHR-Mk1 equilibrium core (last inner iteration of outer iteration 2 during the generation of the equilibrium core presented in Section 4.1). As has been demonstrated for the PBMR-400 slice depletion, the one-group removal cross sections are almost constant over burnup, because the spectral conditions are almost constant during depletion. The composition of most of the fuel pebbles in the slice model does not change during depletion of the surrogate models. The buildup of plutonium over depletion results in stronger self-shielding effects, and only the ^{240}Pu shows a small decrease. However, even this effect is small when compared to the burnup-dependent changes in common LWRs.

Based on this result, it cannot be concluded that burnup dependence does not play a general role in FHRs. However, since the fuel pebbles in the equilibrium core are constantly surrounded by fuel pebbles at different burnups, this can serve as a first indicator that burnup dependence might not be the most important dependence for the one-group cross sections.

7.2 DEPENDENCE OF AXIAL AND RADIAL LOCATION IN THE CORE

Figure 45 shows the one-group removal cross sections for the different axial zones, which are always in the middle radial zone in the equilibrium core. Zone 1 is the bottom of the reactor, and zone 10 is the top (Figure 17). The one-group cross sections are almost constant over the main core region. This is consistent with the findings for the PBMR-400 [Skutnik & Wieselquist, 2021]. Because of the different local moderator-to-fuel ratios in the inlet and outlet regions of the core, significant differences can be observed for the one-group cross sections in these regions. ^{240}Pu shows an opposing trend when compared to ^{235}U, ^{239}Pu, and ^{241}Pu.

Figure 46 shows the one-group removal cross sections for the different radial zones of axial zone 3. As demonstrated for the PBMR-400, the cross sections show a much higher radial variation compared to the axial variation.

In conclusion, for the generation of one-group cross sections, a slice model might be sufficient to cover the main cylindrical region of the reactor. A sufficient radial resolution can ensure consideration of the radial variation. The inlet and outlet regions may require additional sets of cross sections, or the differences may need to be considered in a different way.

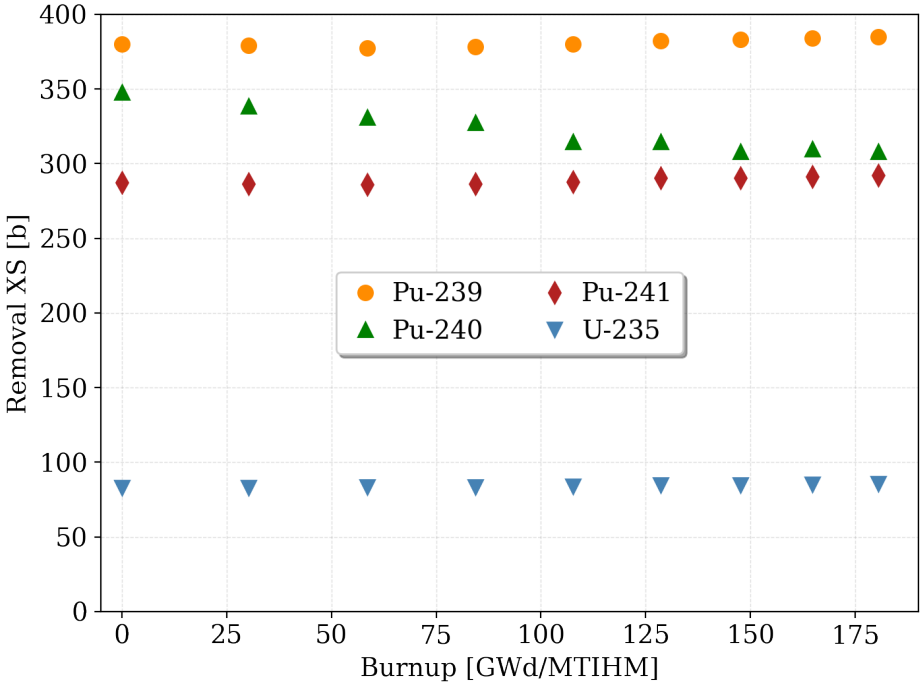

Figure 44. One-group removal cross section as a function of burnup.

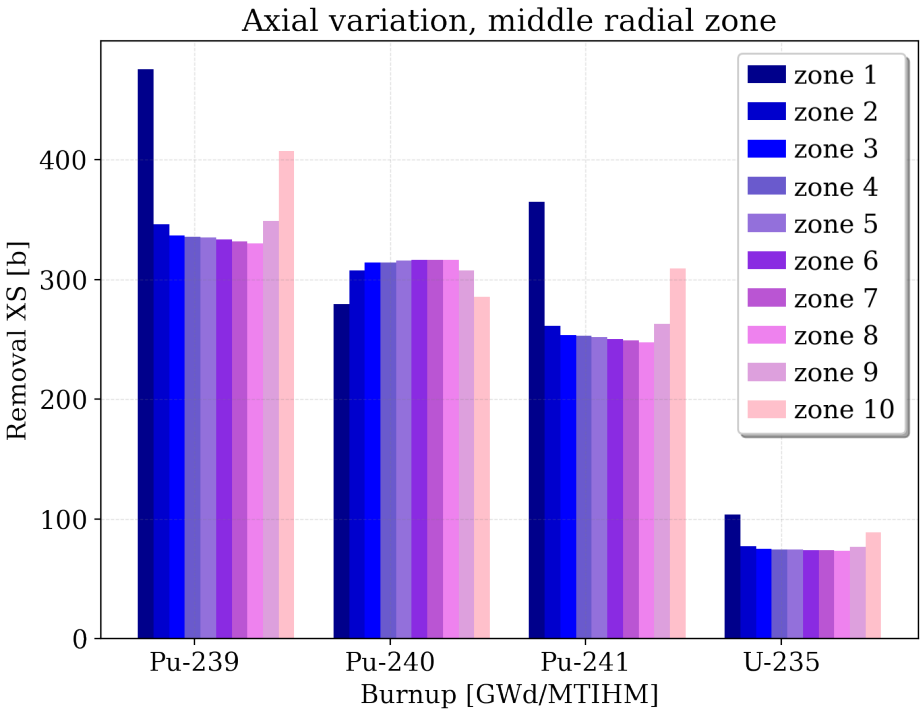

Figure 45. Axial variation of the one-group removal cross section.

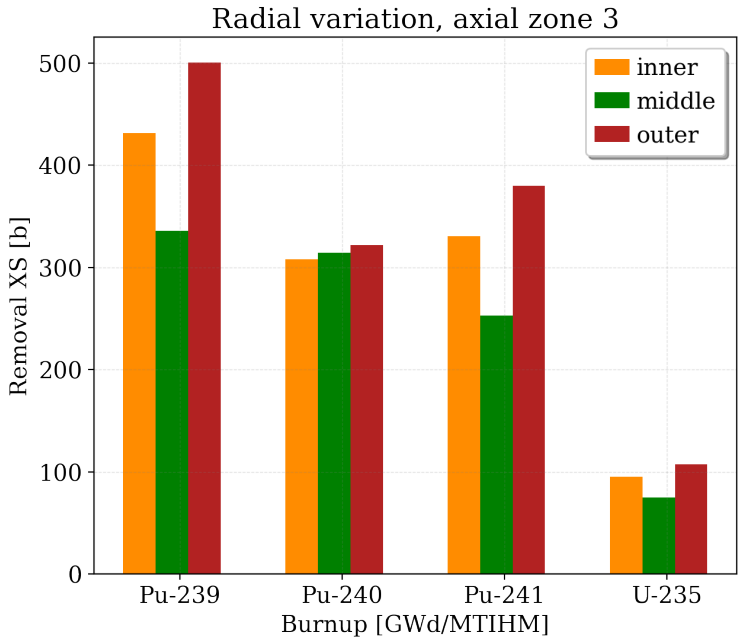

Figure 46. Radial variation of the one-group removal cross section.

8. CONCLUSIONS

As part of an NRC-sponsored project, the SNL MELCOR team and the ORNL SCALE team are collaborating to assess the modeling and simulation capabilities for accident progression, source term, and consequence analysis for non-LWR technologies. SCALE is being used to provide MELCOR with fission product and radionuclide inventories, kinetics parameters, power distributions, and decay heat based on results obtained with the SCALE/TRITON sequence and the depletion solver ORIGEN. With this information, MELCOR can be used to perform severe accident progression and source term analyses. This report summarizes the outcome of the SCALE analyses of the FHR-related studies based on the preconceptual design for a small modular 236 MWth FHR developed by the University of California, Berkeley (PB-FHR-Mk1). The report focuses on the demonstration of SCALE's capabilities for the simulation of this reactor concept. It is noted that an actual safety analysis requires the addition of sensitivity and uncertainty analyses to best-estimate calculations or the consideration of the most conservative conditions.

The applicability of SCALE's MG approach for the simulation of the PB-FHR-Mk1 was confirmed through comparison of MG with reference CE results of single pebble depletion calculations. Very good agreement was obtained, with reactivity differences of less than 260 pcm and differences in the obtained nuclide densities of less than 3% throughout depletion. Based on this good agreement and previous experience gained for HTGR systems, SCALE's MG approach was used for all the calculations of the core slice model and the full core model.

Fuel compositions for the different regions in the full PB-FHR-Mk1 reactor core were developed for the state of equilibrium during which fuel pebbles are continuously added and removed from the core such that the average fuel compositions (and consequently the average burnup) in each core region remains approximately the same. With respect to severe accident analysis, consideration of an equilibrium state as compared to a start-up core or any configuration approaching an equilibrium state was considered the limiting state since the burnup and consequently the decay heat is greater at this stage than compared to any other stage during the run-in phase, during which more fresh fuel pebbles or pebbles with low burnup are included in the core. Using an iterative approach, fuel compositions were determined through interpolation and mixing of burnup-dependent fuel compositions which were obtained through the depletion calculation of a core slice model. Although constant average operating temperatures were applied during in this approach, the relevance of the consideration of temperature distributions for the calculation of fuel compositions at various stages of burnup was pointed out.

The power profile of the equilibrium core showed the highest power in the inner radial region of the cylindrical core. Axially, the normalized power profile showed the maximum value of 2.1 in the third of ten axial zones when counting from bottom to top. This was the result of the increase of burnup with axial core height given the traveling path of the pebbles through the reactor.

The decay heat of the equilibrium core right after shutdown was calculated as ~5.7% of the nominal reactor power. This is slightly smaller than typically found for LWRs and is explained by the differences in the fuel enrichment, maximum burnup, specific power, and power history.

The temperature reactivity feedback was calculated for different components of the reactor at average operating temperatures. In contrast to the approximately linear behavior observed for the salt coolant and the fuel, the moderator and graphite reflector temperature reactivity feedback showed a non-linear behavior. Furthermore, the inner and outer reflector structures show a positive temperature feedback of 1.21 pcm/K and 0.61 pcm/K, respectively, caused by the increase of the neutron scattering cross section of graphite with increasing temperatures; all other feedback effects were found to be negative, as expected. A strong negative

fuel temperature feedback of -3.90 pcm/K and a graphite moderator temperature feedback of -1.10 pcm/K were calculated. For the FLiBe coolant salt surrounding the fuel pebbles, the salt density decrease with increasing temperatures needed to be considered. While the reactivity feedback from only the temperature yielded -0.48 pcm/K, the combined reactivity feedback of the temperature and the density was obtained as -1.56 pcm/K. It was found that the determined reactivity effects are not sensitive to small temperatures perturbations around the average operating temperatures.

The calculation of the tritium production rate in the salt coolant revealed an initial tritium production rate of 0.147 mol/EFPD as a result of the initial large concentration of ^{6}Li in the salt. Because ^{6}Li is depleted and partially replenished through neutron reactions with ^{9}Be, the tritium production rates decreased during operation and approached an equilibrium tritium production rate of 0.021 mol/EFPD after approximately 10 years of full-power operation. A sensitivity calculation revealed that whereas the initial tritium production rate depends on initial ^{7}Li enrichment, the equilibrium tritium production rate is independent of initial ^{7}Li enrichment and is strongly dependent on flux.

A limited analysis of the one-group cross sections resulted in conclusions similar to those from the detailed analysis of the PBMR-400 [Skutnik & Wieselquist, 2021]. Only a minor dependence of the one-group removal cross section on the burnup was observed for the depletion of surrogate fuel pebbles in a core slice model with static representative spectral conditions. Whereas strong radial dependence of the one-group removal cross section in the equilibrium core was observed, axial dependence was limited to only the inlet and outlet regions of the core caused by the changed moderator-to-fuel ratio, and therefore, different spectral conditions in these core region. In addition to the challenges and conditions described by Skutnik and Wieselquist [Skutnik & Wieselquist, 2021], consideration of such regions will provide a challenge for the development of rapid depletion with SCALE's ORIGAMI code. The goal for ongoing development efforts in ORIGAMI include rapid depletion of pebbles while traveling through pebble-bed reactors, and the simplified generation of an equilibrium core based on pre-generated ORIGEN cross section libraries.

The results obtained with SCALE were post-processed to provide the MELCOR team with the core inventory and decay heat of the equilibrium core, a zone-wise power profile, temperature feedback coefficients, the tritium production rate, and the xenon worth for the simulation of an anticipated transient without SCRAM, a station blackout, and a loss-of-coolant accident [Wagner et al., 2021a, Wagner et al., 2021b].

REFERENCES

[Andreades et al., 2016] C. Andreades, et al. (2016). "Design Summary of the Mark-I Pebble-Bed, Fluoride Salt-Cooled, High-Temperature Reactor Commercial Power Plant," *Nuclear Technology*, 195(3), 223–238. doi:10.13182/NT16-2.

[Andreades et al., 2014] C. Andreades, et al. (2014). *Technical Description of the "Mark 1" Pebble-Bed Fluoride-Salt-Cooled High-Temperature Reactor (PB-FHR) Power Plant,* Technical Report UCBTH-14-002, University of California, Berkeley, CA. https://web.mit.edu/nse/pdf/researchstaff/forsberg/FHRPointDesign14-002UCB.pdf.

[ANS Nuclear Newswire, 2021] ANS Nuclear Newswire (2021). "Kairos Power is Building toward Low-Power Demo Operations in 2026," online newspaper article, https://www.ans.org/news/article-3077/kairos-power-is-building-toward-lowpower-demo-operations-in-2026/. Date accessed: August 20, 2021.

[Bostelmann et al., 2020] F. Bostelmann, et al. (2020). "SCALE Capabilities for High Temperature Gas-Cooled Reactor Analysis," *Annals of Nuclear Energy*, 147, 107673. doi:10.1016/j.anucene.2020.107673.

[Choe et al., 2018] J. Choe, et al. (2018). "Fuel Cycle Flexibility of Terrestrial Energy's Integral Molten Salt Reactor (IMSR®)," In *38th Annual CNS Conference and 42nd CNS/CNA Student Conference, Saskatoon, SK, Canada, June 3–6*.

[Cisneros, 2013] A. T. Cisneros (2013). *Pebble Bed Reactors Design Optimization Methods and Their Application to the Pebble Bed Fluoride Salt Cooled High Temperature Reactor (PB-FHR)*. PhD thesis, University of California, Berkeley, https://escholarship.org/uc/item/98384265.

[Goluoglu & Williams, 2005] S. Goluoglu, and M. L. Williams (2005). "Modeling Doubly Heterogeneous Systems in SCALE," In *Transactions of the American Nuclear Society, Vol. 93, ANS Winter Meeting, Washington D.C., November 13–17*.

[Holcomb et al., 2011] D. E. Holcomb, et al. (2011). *Core and Refueling Design Studies for the Advanced High Temperature Reactor* Technical Report ORNL/TM-2011/365, Oak Ridge National Laboratory, Oak Ridge, TN. doi:10.2172/1025857

[Humphries et al., 2015] L. L. Humphries, et al. (2015). *MELCOR Computer Code Manuals Volume 1: Primer and Users' Guide,* Technical Report SAND2015-6691R, Sandia National Laboratories, Albuquerque, NM. doi:10.2172/1433069

[Ilas, 2010] G. Ilas (2010). "On SCALE Validation for PBR Analysis," In *International Conference on the Physics of Reactors, PHYSOR 2010, Pittsburgh, PA, May 9–14*.

[Ilas et al., 2012] G. Ilas, et al. (2012). *Validation of SCALE for High Temperature Gas- Cooled Reactor Analysis,* Technical Report NUREG/CR-7107, ORNL/TM-2011/161, Oak Ridge National Laboratory, Oak Ridge, TN. doi:10.2172/1048709

[Kim et al., 2021] K. S. Kim, et al. (2021). "Improvement of the SCALE-XSProc Capability for High-Temperature Gas-Cooled Reactor Analysis," In *M&C2021, October 3–7, 2021*.

[Krishna et al., 2020] V. Krishna, et al. (2020). "Assembly Design of a Fluoride Salt-Cooled High Temperature Commercial-Scale Reactor: Neutronics Evaluation and Parametric Analysis," *Annals of Nuclear Energy*, 141, 107288. doi:10.1016/j.anucene.2019.107288.

[Lamarsh & Baratta, 2001] J. R. Lamarsh, and A. J. Baratta (2001). *Introduction to Nuclear Engineering*, 3rd edition, Chapter 7. Prentice Hall: Upper Saddle River, NJ.

[NEA, 2013] NEA (2013). *PBMR Coupled Neutronics/Thermal-hydraulics Transient Benchmark, The PBMR-400 Core Design – Volume 1: The Benchmark Definition,* Technical Report NEA/NSC/DOC(2013)10, OECD/NEA. https://www.oecd-nea.org/jcms/pl_19318/pbmr-coupled-neutronics/thermal-hydraulics-transient-benchmark-the-pbmr-400-core-design-volume-1-the-benchmark-definition.

[Romatoski & Hu, 2017] R. R. Romatoski, and L. W. Hu (2017). "Fluoride Salt Coolant Properties for Nuclear Reactor Applications: A Review," *Annals of Nuclear Energy*, 109, 635–647. doi:10.1016/j.anucene.2017.05.036.

[Shen et al., 2019] D. Shen, et al. (2019). *Molten-Salt Reactor Experiment (MSRE) Zero-Power First Critical Experiment with U-235,* Technical Report MSRE-MSR-EXP-001, NEA/NSC/DOC(2006)1, Rev. 0, International Handbook of Reactor Physics Experiments, OECD/NEA.

[Skutnik & Wieselquist, 2021] S. E. Skutnik, and W. A. Wieselquist (2021). *Assessment of ORIGEN Reactor Library Development for Pebble-Bed Reactors Based on the PBMR-400 Benchmark,* Technical Report ORNL/TM-2020/1886, Oak Ridge National Laboratory, Oak Ridge, TN. doi:10.2172/1807271

[Stempien et al., 2016] J. D. Stempien, et al. (2016). "An integrated model of tritium transport and corrosion in fluoride salt-cooled high-temperature reactors (fhrs) – part i: Theory and benchmarking," *Nuclear Engineering and Design*, 310, 258–272. doi:10.1016/j.nucengdes.2016.10.051.

[Sunny & Ilas, 2010] E. E. Sunny, and G. Ilas (2010). "SCALE 6 Analysis of HTR-10 Pebble-Bed Reactor for Initial Critical Configuration," In *International Conference on the Physics of Reactors, PHYSOR 2010, Pittsburgh, PA, May 9–14*.

[Takamatsu et al., 2014] K. Takamatsu, et al. (2014). "Spontaneous stabilization of HTGRs without Reactor Scram and Core Cooling – Safety Demonstration Tests Using the HTTR: Loss of Reactivity Control and Core Cooling," *Nuclear Engineering and Design*, 271, 379–387. doi:10.1016/j.nucengdes.2013.12.005.

[Terry et al., 2007] W. K. Terry, et al. (2007). *Evaluation of the Initial Critical Configuration of the HTR-10 Pebble-Bed Reactor,* Technical Report HTR10-GCR-RESR-001, NEA/NSC/DOC(2006)1, Rev. 0, International Handbook of Reactor Physics Experiments, OECD/NEA.

[US NRC, 2020] US NRC (2020). *NRC Non-Light Water Reactor (Non-LWR) Vision and Strategy, Volume 3: Computer Code Development Plans for Severe Accident Progression, Source Term, and Consequence Analysis,* Technical Report ML20030A178, Rev. 1, US NRC, Rockville, MD. https://www.nrc.gov/docs/ML2003/ML20030A178.pdf.

[Wagner et al., 2021a] K. Wagner, et al. (2021a). *MELCOR Accident Progression and Source Term Analysis for a Fluoride High-Temperature Reactor,* Technical Report SAND2021-11113 PE, Sandia National Laboratories, Albuquerque, NM.

[Wagner et al., 2021b] K. Wagner, et al. (2021b). *MELCOR FHR Demonstration Source Term Calculation,*. Technical report Sandia National Laboratories, Albuquerque, NM.

[Walker et al., 2021] E. Walker, et al. (2021). *SCALE Modeling of the Fast-Spectrum Heat Pipe Reactor,* Technical Report ORNL/TM-2021/2021, Oak Ridge National Laboratory, Oak Ridge, TN.

[Wieselquist et al., 2020] W. A. Wieselquist, et al. (2020). *SCALE Code System, Version 6.2.4,* Technical Report ORNL/TM-2005/39, Oak Ridge National Laboratory, Oak Ridge, TN. https://www.ornl.gov/file/scale-62-manual/display.

[Williams, 2011] M. L. Williams (2011). "Resonance Self-Shielding Methodologies in SCALE 6," *Nuclear Technology*, 174, 149–168. doi:10.13182/NT09-104.

[Williams et al., 2015] M. L. Williams, et al. (2015). "A New Equivalence Theory Method for Treating Doubly Heterogeneous Fuel - I: Theory," *Nuclear Science and Engineering*, 180, 30–40. doi:10.13182/NSE14-68.